

FRACTAL-BASED MAGNETIC RESONANCE IMAGING COILS FOR 3T XENON IMAGING

FRACTAL-BASED MAGNETIC RESONANCE IMAGING COILS FOR
3T XENON IMAGING

By Jimmy NGUYEN

*A Thesis Submitted to the School of Graduate Studies in the Partial
Fulfillment of the Requirements for the Degree Master of Applied Science*

McMaster University © Copyright by Jimmy NGUYEN 10 July 2020

McMaster University

Master of Applied Science (2020)

Hamilton, Ontario (Department of Electrical & Computer Engineering)

TITLE: Fractal-based magnetic resonance imaging coils for 3T Xenon imaging

AUTHOR: Jimmy NGUYEN, B.Eng., (McMaster University)

SUPERVISOR: Dr. Michael D. NOSEWORTHY

NUMBER OF PAGES: ix, 77

Abstract

Traditional ^1H lung imaging using MRI faces numerous challenges and difficulties due to low proton density and air-tissue susceptibility artifacts. New imaging techniques using inhaled xenon gas can overcome these challenges at the cost of lower signal to noise ratio. The signal to noise ratio determines reconstructed image quality and is an essential parameter in ensuring reliable results in MR imaging. The traditional RF surface coils used in MR imaging exhibit an inhomogeneous field, leading to reduced image quality. For the last few decades, fractal-shaped antennas have been used to optimize the performance of antennas for radiofrequency systems. Although widely used in radiofrequency identification systems, mobile phones, and other applications, fractal designs have yet to be fully researched in the MRI application space. The use of fractal geometries for RF coils may prove to be fruitful and thus prompts an investigation as the main goal of this thesis. Preliminary simulation results and experimental validation results show that RF coils created using the Gosper and pentaflake offer improved signal to noise ratio and exhibit a more homogeneous field than that of a traditional circular surface coil.

Acknowledgements

First and foremost, I would like to thank my supervisor Michael D. Noseworthy for all of his countless hours spent reading, reviewing, and suggesting edits in the production of this thesis. Without his help and suggestions this project would have not been a success. My grateful thanks also extends to Dr. Natalia Nikolova for allowing my use of her software licenses for analysis and simulations. I probably racked up a thiccccc electricity bill running those servers at maximum capacity for weeks at a time. I would also like to thank Norm Konyer for guiding me and his expertise in the design and construction of RF coils, especially in the context of xenon imaging. Without the financial support of Dr. Pedram Yazdanbakhsh and Ceresensa Inc., in addition to MITACS, this project would not have been possible and I would like to express my thanks and gratitude for their support in the undertaking of this thesis. Finally, a gracious thank you also goes out to the technical staff at the Imaging Research Center for assisting and training me in the use of the MRI.

Cheers to my lab colleagues for the fun trivia hangouts. And dealing with my obviously embellished clearly-didn't-happen stories. Or trying to interpret the ridiculous corruption of English I always speak. Or hearing me talk relentlessly about [cooking, fishing, my lifeless garden, the non-existent soon™ 1977 Cutlass Supreme]. If you're reading this, you know who you are. Although I miiiiight just be too lazy to write everyone's name down. Thesis writers HATE this one trick! If you don't do any shoutouts in the acknowledgements, then nobody can be mad for being left out. Beer's on me if you actually end up reading this though.

Ashley.

Contents

Abstract	iii
Acknowledgements	iv
1 Introduction	1
1.1 Background	1
1.2 Motivation	3
1.3 Contributions	3
1.4 Outline of Thesis	4
2 Background	5
2.1 Magnetic resonance imaging	5
2.1.1 Signal source	5
2.1.2 Applied radiofrequency pulse	8
2.1.3 Image generation	10
2.1.4 Pulse sequences	13
2.1.5 Xenon MR Ventilation Imaging	15
2.2 Radiofrequency coils	17
2.3 Fractal antennas	21
3 Design Methodology and Simulations	26
3.1 Design Methods, Materials and Methodology	27
3.1.1 Fractal design selection	29
3.2 Simulations	32
3.2.1 Metrics for Tuning, Matching and Field Measurements	34
3.2.2 Simulation Results	37
4 Fabrication and Experimental Procedure	38
4.1 Fabrication	38
4.2 MRI SNR evaluation	43
5 Performance Evaluation	47

5.1	Simulation Performance Results	47
5.1.1	Magnetic field analysis	48
5.2	Experimental Results	59
5.2.1	Fabricated Coil Analysis	59
6	Conclusion and Future Work	63
6.1	Future Improvements	64
A	Chapter 3 Supplement	66
A1	OpenSCAD L-system generator	66
	Bibliography	74

List of Figures

2.1	Circuit model of a resonant LC circuit, depicting an RF coil with resistance and inductance, with tuning and matching capacitors	17
2.2	Fractals - A: Sierpinski arrowhead, levels 2, 3; B: Peano curve; C: Hilbert curve, levels 4, 5; D: Gosper arrowhead; E: n-flake “pentaflake”, levels 2, 3; F: Gosper island curve; G: Koch snowflake, levels 2, 3; H: Moore curve	23
3.1	RF coil design methodology workflow	28
3.2	Gosper island fractal, level 3	31
3.3	n-flake “pentaflake” fractal, level 2	31
3.4	Sierpinski arrowhead fractal, level 4	32
3.5	Reference coil	32
4.1	PCB layer stackup. Silkscreen overlay (top and bottom) are produced using non-conductive UV-cured epoxy ink.	40
4.2	Image of impedance measurement setup using the Agilent 4395A	43
4.3	Image of impedance measurement setup using the nanoVNA	44
4.4	Image of online calculator used to achieve preliminary match (Analog Devices 2020)	45
4.5	Images of constructed PCB coils - Top-left: Reference, top-right: Sierpinski, bottom-left: Pentaflake, bottom-right: Gosper	46
5.1	S11 (dB) reflection coefficient measurements for simulated coils in HFSS. top-left: reference, top-right: Gosper, bottom-left: pentaflake, bottom-right: Sierpinski	48
5.2	Image of ROI for each coil - Top-left: Reference, top-right: Sierpinski, bottom-left: pentaflake, bottom-right: Gosper	49
5.3	Bartlett test for the mean of the magnetic field, ROI slices in the z-direction	50
5.4	Levene test for the mean of the magnetic field, ROI slices in the z-direction	51

5.5	Simulated H-field strengths of each coil, in ROI slices in the z-plane direction	52
5.6	2D contour plot of H field in xy plane, z = 10 mm	53
5.7	2D contour plot of H field in xy plane, z = 20 mm	54
5.8	2D contour plots of H field in xz plane, y = 50 mm	55
5.9	2D contour plots of H field in yz plane, x = 50 mm	56
5.10	Coefficients of variation of each coil as a function of distance from the xy-plane in the z-direction	57
5.11	Maximum electric field (V/m) as a function of distance from the z-plane (mm)	58
5.12	Comparison of S11 (dB) measurement of constructed coils using both NanoVNA and Agilent 4395A, top-left: reference, top-right: Sierpinski, bottom-left: pentaflake, bottom-right: Gosper	60
5.13	Comparison of impedance measurement (Smith chart) of constructed coils using both NanoVNA and Agilent 4395A, top-left: reference, top-right: pentaflake, bottom-left: Sierpinski, bottom-right: Gosper	61
5.14	Comparison of FID signal power spectra, with measures of SNR between each coil	62

List of Tables

2.1	Table of common nuclei used in MRI listing Larmor resonance frequencies in Hz and rad s^{-1} . f_{Larmor} are for nuclei in a field of 3 T. Negative precessional frequencies indicate spin angular momentum precession in a counter-clockwise rotation, opposite to the positive clockwise convention.	8
5.1	Table of ROI dimensions for each coil	49
5.2	Table of means, standard deviations and coefficients of variation for simulated H fields for fractal and reference coils at $z = 10$ mm and 20 mm	52
5.3	Table of maximum electric field strength (V/m) for fractal and reference coils	59
5.4	Table of measured SNR results for each coil	60

Chapter 1

Introduction

1.1 Background

Magnetic resonance imaging (MRI) technology has long been used to visualize the structure of the brain, heart, joints, and various organs within the body. The chest and lungs are of particular interest. Standard lung imaging is done through computed tomography (CT) scanning at the risk of exposing a patient to ionizing radiation. Because MRI does not involve ionizing radiation there is considerable interest in its utility for lung imaging. However, image quality within this region is reduced due to magnetic susceptibility artifacts caused by tissue-air interfaces as well as low ^1H proton density within the lungs (Biederer et al. [2012](#)). Alternatively, because there are other nuclei, besides ^1H which have the quantum mechanical property of spin necessary for visibility with MRI, focus has shifted away from conventional MRI approaches to more novel ones. Still, however, non-proton based imaging has the challenge of lower SNR. This can be alleviated through hyperpolarized gas MRI (discussed later). The use of hyperpolarized gases such as helium-3 (^3He) and xenon-129 (^{129}Xe) can provide higher signal

from airways and spaces within the lungs. This procedure is called ventilation imaging. In addition to structural information, hyperpolarized gas MRI can also be used to obtain functional performance characteristics of the pulmonary system (Biederer et al. 2012).

The signal-to-noise ratio (SNR) of MR imaging is linked to radio frequency (RF) detector coil performance. RF surface coil designs used in MRI applications exhibit an inhomogeneous RF transmit field (called B_1^+) and thus improvements in coil design to reduce inhomogeneity may lead to improved image quality.

Fractal-shaped radio frequency antennas are a modern innovation in antenna engineering. A fractal – a structure with an embedded self-similar structure at a multiple scales – is used as the geometric foundation in small-scale antennas because the fractal structures provide similar if not better performance to standard antenna designs in limited space applications (Cohen 1995). Fractal antennas have also successfully been applied to near-field RF identification systems (Pakkathillam et al. 2013).

This thesis builds upon previous work (Lemus et al. 2018) in which simulations of Koch-shaped fractal coils were shown to have an increased magnetic field strength when compared to a standard circular coil. The Koch-shaped fractal coil also had a more uniform magnetic field distribution, which may lead to an improvement in image quality. The relatively small amount of research in the application of fractal-geometry shaped coils to MRI spurred the undertaking of this thesis. Thus the goal of this thesis was to examine the effects of different fractal-shaped RF coils when used in a ^{129}Xe xenon-focused MRI application. Xenon MRI scanning was chosen because, although important for lung MRI, the method typically suffers from poor SNR, and ΔB_1^+ relative

to routine ^1H MRI.

1.2 Motivation

The work presented in this thesis explores a niche facet of RF engineering and integrates it into the field of magnetic resonance imaging (MRI). By combining together fractal geometries commonly used in antenna designs with the application of RF surface coils in MRI, new insights can be gained in MRI surface coil design and performance. Furthermore, if successful the concepts could be integrated into volume coils for larger tissue coverage.

1.3 Contributions

The author has contributed to the development of RF coils in the field of magnetic resonance imaging in the following ways:

1. Provided a design methodology for the simulation, fabrication, and verification of RF coils
2. Examined the efficacy of fractal-geometry in the application of magnetic resonance imaging coils
3. Characterized the effects of fractal shapes and on the electric and magnetic field strength and homogeneity produced by an RF coil

1.4 Outline of Thesis

This thesis presents work performed in designing, simulating, fabricating, and verifying the performance characteristics of fractal-shaped surface coils in the context of 3T ^{129}Xe MRI.

Chapter 2 discusses the background of MRI physics, the concept of magnetization and how signals are acquired using RF coils. Additionally, the chapter discusses RF coil theory and how fractal designs in RF antenna engineering may be applied to coil designs in MRI.

Chapter 3 outlines the complete design methodology, as well as the simulation component of the RF coil designs. Each RF coil design will be simulated in software and the designs of each fractal discussed.

Chapter 4 outlines the fabrication and measurement methods for the fractal-based RF coils. Details on the materials and justification for design decisions are discussed.

Chapter 5 discusses the performance of fabricated coils and compares the measured parameters of coils to their simulation. Differences between the simulation and measured results will be discussed.

Chapter 6 summarizes the work of the thesis and highlights the major results. The chapter also provides areas of improvements and suggestions for future work.

Chapter 2

Background

2.1 Magnetic resonance imaging

2.1.1 Signal source

Magnetic resonance imaging (MRI) uses the quantum property of spin angular momentum of an atomic nucleus, a magnetic field, and RF pulses to generate a signal. The signal is spatially encoded using three orthogonally applied magnetic field gradients leading to a resulting image. As a simplification, the spin angular momentum of an atomic nucleus – spin – is commonly represented as a spinning charged sphere with angular momentum, J , and a vector denoting the nuclear magnetic moment, μ . Nuclei placed into an environment without a magnetic field have their spins randomly oriented, and have no net magnetic moment (M).

There are two overall approaches to describing MRI: one is a quantum mechanical approach, while the other approach is a Newtonian perspective and involves simplified representations using spinning vectors. With the exception of the most basic elements

of the signal, the bulk of the MRI description will be focused on the Newtonian or classical mechanical description.

In the quantum mechanical description of MRI, an externally applied magnetic field (B_0) will cause the the spins within the sample to split their energy levels into a higher, anti-parallel ($-\frac{1}{2}$) and lower, parallel ($+\frac{1}{2}$) state. The difference in energy levels between the two states is described by the following relation:

$$\Delta E = \hbar\gamma B_0 \quad (2.1)$$

where \hbar is the reduced Planck constant ($J \cdot s$), γ is the gyromagnetic ratio (explained later), and B_0 , the externally applied magnetic field strength (T).

The energy of a photon can be described using the Planck relation as:

$$\Delta E = \hbar f_0 \quad (2.2)$$

This relation was originally derived in order to explain the splitting of spectral lines of light in a magnetic field, however the eventual discovery of nuclear magnetic resonance found that this relation also applies in that context.

Of the two energy states at room temperature, the lower energy level will have a slightly higher amount of spins. The ratio of spins in each state can be described using

the Boltzmann distribution:

$$\frac{N^+}{N^-} = \exp\left(-\frac{\Delta E}{kT}\right) \quad (2.3)$$

where k is the Boltzmann constant (J K^{-1}), and T is the temperature of the system in Kelvin.

In the quantum description, when a sample is placed into an externally applied magnetic field (B_0), the random orientations of the nuclear spins align such that there is a statistically significant number in parallel and anti-parallel orientations, with respect to the direction of the field. A small number of these spins will be more aligned in the parallel orientation than anti-parallel orientation due to a lower energy state in that orientation. From the Newtonian description it is then said that this imbalance leads to a net magnetic moment. Furthermore, the presence of the magnetic field leads to precession of the nucleus at a frequency known as Larmor frequency.

By combining the Planck (2.2) and Zeeman (2.1) relations together, the Larmor precession frequency can be derived as:

$$f_{Larmor} = \frac{\gamma}{2\pi} B_0 \quad (2.4)$$

Where γ is a parameter known as the gyromagnetic ratio. The gyromagnetic ratio is an intrinsic property of the nucleus in question, defined by the ratio of the magnetic moment and angular momentum. The units thus are $\frac{\text{rad}}{\text{s T}}$. For a ^1H atom,

Nuclei	γ (MHz T ⁻¹)	γ (rad s ⁻¹ T ⁻¹)	f_{Larmor} (MHz)	f_{Larmor} (rad s ⁻¹)
¹ H	42.58	267.52	127.74	802.56
³ He	-32.43	-203.79	-97.29	-611.29
¹³ C	10.71	67.28	32.13	201.87
¹⁹ F	40.05	251.66	120.15	754.92
²³ Na	11.26	70.76	33.78	212.24
³¹ P	17.24	108.29	51.72	324.96
¹²⁹ Xe	-11.77	-73.99	-35.31	-221.86

TABLE 2.1: Table of common nuclei used in MRI listing Larmor resonance frequencies in Hz and rad s⁻¹. f_{Larmor} are for nuclei in a field of 3 T. Negative precessional frequencies indicate spin angular momentum precession in a counter-clockwise rotation, opposite to the positive clockwise convention.

$\gamma \approx 42.576 \text{MHz T}^{-1}$ and thus the precessional frequency of ¹H atoms within a 3T – a common clinical field strength – magnet is $\approx 128 \text{MHz}$.

Table 2.1 lists the common nuclei of interest used in MRI, along with their gyromagnetic ratio and resonance frequencies at 3 T.

2.1.2 Applied radiofrequency pulse

When a radiofrequency pulse, at a frequency coinciding with the product of γ and B_0 , is applied to the nuclear spins, the spins will absorb the RF energy. The energy is emitted from the spins as they return to thermal equilibrium, the energy of which can be detected. The application of the radiofrequency pulse creates a local transmitted magnetic field denoted B_1^+ , which leads to the net magnetization of the spins to tip from the parallel direction. In the MR context, the static magnetic field is oriented along z , typically down the magnet bore. The applied RF pulse is delivered such that a component of the resultant net magnetization vector projects to the transverse plane (i.e. will tip into the xy plane). The net magnetization of these spins is represented by

M.

The amount by which the net magnetization vector tips transversely toward the xy plane is described using:

$$\theta = \gamma B_1^+ t_p \quad (2.5)$$

where θ is the tip angle, and t_p is the duration of applied radiofrequency pulse. This equation is only an approximation for rectangular “hard” pulses and for other radiofrequency waveforms, other equations may be used (Brown et al. 2014). The maximal signal is seen at a tip angle of 90° , as that is when the net magnetization moment is directed completely into the transverse plane.

The perturbation of the net magnetization vector into the transverse plane can be described by the solutions to the set of Bloch equations. The Bloch equations are used to determine the net magnetization of a system as a function of time, with differing solutions accounting for higher-order interactions between the spins – such as diffusion in the generalized Bloch-Torrey equation. In the simplified case of spins within a magnet, the solutions are:

$$M_x(t) = M_0 \exp\left(-\frac{t}{T_2}\right) \sin(\omega t) \quad (2.6)$$

$$M_y(t) = M_0 \exp\left(-\frac{t}{T_2}\right) \cos(\omega t) \quad (2.7)$$

$$M_z(t) = M_0 \left(1 - \exp \left(-\frac{t}{T_1} \right) \right) \quad (2.8)$$

where T_1 and T_2 are parameters known as relaxation times. Relaxation times are decay constants which describe the change in magnetization (signal) towards its equilibrium value, before the pulse was applied. At a particular field strength these constants are tissue-dependent and are derived experimentally. The T_1 constant describes the growth or return of the magnetization from the transverse plane as it returns to the parallel (B_0) orientation. The T_2 constant describes how the individual spins that comprise the net magnetization moment dephase from one another.

2.1.3 Image generation

The Bloch equation solutions in 2.6 and 2.7, are the signals produced by the nuclear spins when excited by a radiofrequency pulse. This signal is termed the free induction decay (FID). By itself however, this signal is not sufficient enough to produce an image. In the imaging process, a secondary magnetic field – called the gradient field – is applied to the nuclear spins along combinations of three orthogonal directions. In general, a single magnetic field gradient induces a spatial linear change in the magnetic field strength across the spins, thus leading to a spatial variation in the Larmor frequency. The deviation in frequency caused by the gradients is only a few hundred to a few thousand Hertz.

Gradients are applied in three orthogonal directions, each with their own gradient coils. These gradients are individually excited in order to image in the axial (via the G_x), coronal (via the G_y), and sagittal (via G_z) planes of anatomy.

The deviation in frequency due to an applied gradient (G_i) in each direction (i) is:

$$G_x = \frac{\delta B_z}{\delta x}, G_y = \frac{\delta B_z}{\delta y}, G_z = \frac{\delta B_z}{\delta z} \quad (2.9)$$
$$f_{Larmor} = \gamma(B_0 + i \cdot G_i)$$

The variation in frequency of the spins can be utilized to determine their position in space, in a process known as slice-selection. Like the keys on a piano keyboard, the spins with a lower resonance frequency will be located “lower” relative to the location where the magnetic field is stronger. This can be combined with the phase differences induced by the gradients in order to produce an image.

During the acquisition step, the digitized signals recorded by the MRI will be a linear combination of these frequency and phase-encoded spins. After filtering and decimation steps, this signal is ordered into a two-dimensional matrix via a formalism known as k-space. k-space holds the received signal until it is reconstructed into an image via the two-dimensional inverse Fourier transform. The outer regions of k-space hold high-frequency components of the reconstructed image, while the center holds the low-frequency components. Similar to image processing, the high-frequency components of k-space correlate to the sharp rises in image space such as edges and boundaries between high and low contrast. The low-frequency components of k-space near the center corresponds to the bulk of the reconstructed image, representing contrast and defining the signal-to-noise ratio.

The encoding of the acquired signal into k-space can be performed with many different methods. The encoding method chosen depends on the performance required – encoding methods will vary the acquisition time, and thus signal-to-noise ratio and

final reconstructed image resolution. A Cartesian trajectory encodes the signal in a grid-like left-to-right, up-to-down direction. More advanced encodings of k-space can vary the trajectory into a radial, spiral, or even pseudo-random directions. These trajectories can trade-off k-space sample points into a higher density near the center, thus leading to increased signal-to-noise ratio at the cost of losing some detail at the edges of anatomical structures.

The MRI signal obtained from the magnetization, M , and within a volume, V :

$$s_r(t) = \int_V M(\vec{r}, t) dV \quad (2.10)$$

By expanding the integral into three dimensions and applying a time-varying gradient, equation 2.10 becomes:

$$s_r(t) = \int_x \int_y \int_z M(x, y, z, 0) e^{(-j\omega_0 t)} \exp\left(-j\gamma \int_0^t \vec{G}(\tau) \cdot \vec{r} d\tau\right) dx dy dz \quad (2.11)$$

By slicing in the the z -direction ($m(x, y) = \int_{z_0-\delta z/2}^{z_0+\delta z/2} M(\vec{r}, t) dz$), and demodulating (by multiplying by $\exp(j\omega_0 t)$), equation 2.11 is thus:

$$s_r(t) = \int_x \int_y m(x, y) e^{(-j\omega_0 t)} \exp\left(-j\gamma \int_0^t \vec{G}(\tau) \cdot \vec{r} d\tau\right) dx dy \quad (2.12)$$

And given the gradient G has orthogonal components G_x and G_y , the signal equation 2.12 becomes:

$$\begin{aligned}
 s(t) &= \int_x \int_y m(x, y) \exp \left(-j\gamma \int_0^t \vec{G}(\tau) \cdot \vec{r} d\tau \right) dx dy \\
 &= \int_x \int_y m(x, y) \exp \left(-j\gamma \int_0^t [G_x(\tau) + G_y(\tau)] d\tau \right) dx dy \quad (2.13) \\
 &= \int_x \int_y m(x, y) \exp \left(-j2\pi(k_x(t)x + k_y(t)y) \right) dx dy
 \end{aligned}$$

where $k_i(t) = \frac{\gamma}{2\pi} \int_0^t G_i(\tau) d\tau$ is the k-space signal for a given direction i . The equation in 2.13 is precisely the two dimensional Fourier transform of the signal in image-space and thus the image obtained from the digitized signals in k-space can be reconstructed via the use of the inverse Fourier transform.

2.1.4 Pulse sequences

Recall that a radiofrequency pulse produces a signal by “tipping” the net magnetization moment into the transverse plane. In equation 2.5, a “hard” pulse is applied to tip the nuclear spins of the sample into the transverse plane. A hard pulse is the equivalent of a continuous wave pulse in radio telecommunications engineering – a sine wave that is pulsed on and off and contains only a single frequency component. Hard pulses are used mainly to excite a whole volume without using any applied gradients. However, the slice selection process uses gradients to selectively excite spins and thus allows for the ability to encode acquired data within k-space for image reconstruction. A hard pulse however contains only one frequency and thus the spins with resonance deviations above and below the Larmor frequency cannot be excited. The shape of the pulse must be modified in order to excite the spins. The most simple method is to define

a rectangular bandwidth of interest in the frequency domain (enveloping the resonance frequencies of the spins within the slice) and then use the inverse Fourier transform to obtain a time-domain signal that can be used as the radiofrequency pulse. This procedure results in a radiofrequency pulse with the shape of a sinc wave. Equation 2.14 describes the sinc pulse that results from this procedure.

$$B_1(t) = A \frac{\sin \Delta f \pi t}{\Delta f \pi t} \sin(2\pi f_L t) \quad (2.14)$$

where A is an arbitrary amplitude factor scaling the voltage of the signal and thus emitted radiofrequency energy, Δf is the desired frequency deviations to capture the spins – commonly denoted as *transmit bandwidth*, and f_L , the Larmor frequency. Mathematically, the sinc pulse is infinite in duration and thus the process of apodization – applying a digital filter to limit the sidelobes of the sinc pulse – is applied in order to truncate the radiofrequency pulse to an acceptable length. More advanced pulse shapes that can include Gaussian-shaped pulses or pulses generated by orthogonal polynomials via the Shinnar-Le Roux (SLR) algorithm (Brown et al. 2014). Note that the *receive bandwidth* (RBW) is an MRI scanner dependent parameter and depends on the hardware used in the radiofrequency frontend of the scanner. The RBW is selectable in order to increase or decrease acquisition time at the cost of signal-to-noise ratio and image quality.

The applied radiofrequency pulse can be applied in multiple repetitions and patterns forming what is known as a *pulse sequence*. TE and TR are parameters in a pulse sequence which describe the echo time and repetition time respectively. In a *spin echo* pulse sequence, an initial radiofrequency pulse tips the spins from parallel, to 90° into

the transverse plane. After a time t , the spins start to dephase and a second radiofrequency pulse is applied. This second pulse is designed to tip the spins 180° , which will cause the spins to rephase and thus a signal can be acquired at time $TE = 2t$. In a *gradient echo* pulse sequence, a dephasing gradient is applied to the spins leading to a faster dephasing of the spins. A rephasing gradient is applied at the same strength but opposite polarity to cause those dephased spins to rephase at time TE . For either of these sequences, a complete repetition of the sequence occurs at time TR . The combination of applied radiofrequency pulses and gradient application in a pulse sequence fills out k-space and thus pulse sequences play a major role in the procedure of image generation for an MRI system.

2.1.5 Xenon MR Ventilation Imaging

Routine clinical MRI uses the proton (^1H) as the signal source. In the lungs, the low proton density leads to a far weaker signal than when compared to other tissues. The proton density within healthy lung tissue is 0.1 g cm^{-3} , which is approximately ten times lower than in other tissue by comparison (Biederer et al. 2012). Additionally, deoxyhemoglobin is paramagnetic but it switches to being diamagnetic when bound to oxygen within tissue. This difference in magnetism leads to susceptibility variations along the air-tissue interface, leading to difficulties in imaging the lung tissue in that region. However, the use of a nuclei other than ^1H can avoid these issues. The use of inhaled hyperpolarized gases such as ^{129}Xe and ^3He as a contrast agent can overcome issues by imaging the airways instead of the tissues, thus avoiding the magnetic susceptibility artifacts. Additionally, the gas is hyperpolarized, thus making the signal-to-noise ratio of the image virtually independent of the main B_0 field.

Hyperpolarization is a technique whereby the the nuclear spins of the gas is biased into the parallel or anti-parallel orientation without the necessity of the main B_0 field. This is used to overcome the inherent low signal-to-noise ratio due to the low density of the gas. A gas can become hyperpolarized through various mechanisms, but the major method is via spin-exchange optical pumping (Walker 2010). Spin-exchange optical pumping can polarize both ^3He and ^{129}Xe , whereby an infrared laser emits circularly polarized light onto an alkali metal such as rubidium. The circularly polarized light will excite electrons of the rubidium atoms, and when the gaseous molecules collide with the rubidium sample, the angular momentum of the spin of the electron will be transferred to the molecule. This transfer of spin causes the gas to become selectively polarized into a spin-up or spin-down state independent of the B_0 field.

The use of ^{129}Xe over ^3He offers many significant advantages. In practical terms, ^3He is relatively scarce, and its use in radiation detectors has substantially increased the price in recent years. This is in contrast to the more inexpensive and naturally abundant ^{129}Xe . For imaging, ^{129}Xe is soluble in pulmonary tissues, giving it a different resonance depending on the tissue in which it is dissolved. ^{129}Xe is detectable in red blood cells, pulmonary tissue, and within the airways, giving three resonant frequencies (Roos et al. 2015). The differing resonant frequencies allows not only the structure of the airways to be determined, but also functional and performance characteristics of the lung may also be assessed as the dissolving of ^{129}Xe and passage through alveolar walls into the bloodstream, is indicative of lung health. It should be noted that ^3He does not dissolve into tissues and blood and hence it only provides a map of the airways down to the alveoli.

2.2 Radiofrequency coils

A radiofrequency coil used in MR signal acquisition is a resonant circuit formed from a loop of conducting material. The loop is usually formed from wire and has an intrinsic inductance (L_{Coil}) and resistance (R). The loop is tuned (explained later) using a tuning capacitor (C_{tune}) and matching capacitor (C_{match}). Figure 2.1 depicts a circuit-level model of an RF coil used in MR imaging.

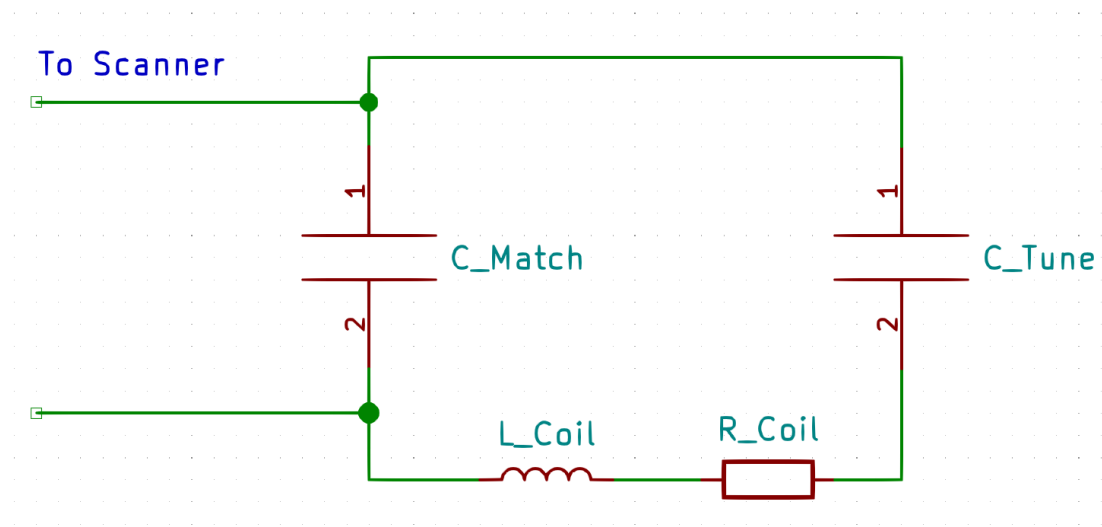


FIGURE 2.1: Circuit model of a resonant LC circuit, depicting an RF coil with resistance and inductance, with tuning and matching capacitors

Standard MRI surface coil geometries are usually circular loops, which produce a magnetic field within the central region of the loop (Vaidya et al. 2016). This generated magnetic field – called the B_1^+ field in the MRI parlance – must have a field that is homogeneous: that is it must have an even distribution of the magnetic field over the region of interest. The traditional circular loop emits an inhomogeneous field, which will lead to local variations in the magnetic field, thus affecting the ability to spatially localize the location of the nuclear spins. The B_1^+ field is stronger in the regions closest to the wire loop, resembling a toroidal shape. The inhomogeneity effect is exacerbated

at high magnetic field strengths and Larmor frequencies, as the higher electromagnetic wave frequencies lead to higher conduction currents within the tissue, causing a greater asymmetry between the B_1^+ transmit and B_1^- receive field (Vaidya et al. 2016; Keltner et al. 1991). The inhomogeneous field leads to artifacts in the reconstructed image, decrease in signal-to-noise ratio and thus reduced image quality.

The majority of RF surface coils used in magnetic resonance imaging are loops formed from wire or copper strips. Coils created using different materials may suit unique problem spaces. For example, stitched conductive thread (Vincent and Rispoli 2019) and screen printing (Corea et al. 2017) have been researched in order to be used in flexible, body-conforming coils. The use of copper foil tape in place of wire loops allow the ease of soldering surface-mount devices such as diodes, inductors and capacitors (Fujita et al. 2013). The use of printed circuit boards (PCBs) is a further advancement of adhesive-backed copper foil, allowing precise control of trace geometry and even allows the use of microstrip tuning stubs in place of physical capacitors or inductors. The fibreglass backing of a printed circuit board also provides mechanical stability to the coil.

The magnetic field produced (B_1^\pm field) at a point by a simple loop of wire with constant current (I) can be derived using the Biot-Savart law as:

$$d\vec{B}_1^\pm = \frac{\mu_0}{4\pi} I \frac{d\vec{s} \times \vec{r}}{r^3} \quad (2.15)$$

where μ_0 is the permeability of free space ($1.257 \times 10^{-6} \text{ T m A}^{-1}$), ds is a differential element along the curvature of the loop, and \vec{r} is a vector towards the point in free

space.

Recall that the free induction decay (FID) magnetization solution to the Bloch equations in equations 2.6 and 2.7 describes the signal as it is generated by the magnetization of the nuclear spins tipping into the transverse plane. This time-varying magnetic flux ($\phi(t)$) induces a voltage in the receive coil and can be derived using Faraday's law as:

$$EMF_{induced} = -\frac{\partial\phi(t)}{\partial t} = -\frac{\partial}{\partial t} \int_{sample} \mathbf{B}_1^-(\vec{r}) \cdot \mathbf{M}_{xy}(\vec{r}) d^3r \quad (2.16)$$

where \int_{sample} is the volume of the sample, and \mathbf{B}_1^- is implicitly defined as the received magnetic field produced per unit current in the loop.

\mathbf{B}_1^+ and \mathbf{B}_1^- distinction

The \mathbf{B}_1^\pm field is generated by a coil is caused by the current passing through the coil as seen in the Biot-Savart derivation in equation 2.15. The \mathbf{B}_1^\pm field is a circularly-polarized field that is the sum of two separate circularly-polarized fields, \mathbf{B}_1^+ and \mathbf{B}_1^- (Vaidya et al. 2016). \mathbf{B}_1^+ is commonly denoted as the transmit field, while \mathbf{B}_1^- is denoted as the receive field. With a linearly-polarized surface coil such as the one used in MRI, the \mathbf{B}_1^\pm field is also linearly polarized and thus \mathbf{B}_1^\pm can be decomposed into equal components of \mathbf{B}_1^+ and \mathbf{B}_1^- . Additionally, the reciprocity theorem in classical electromagnetics can be applied to show that the \mathbf{B}_1^+ and \mathbf{B}_1^- fields are the same. The reciprocity theorem allows for the interchange of electrical currents and generated electric and magnetic fields without a change in the field characteristics. For example, the magnetic field produced at a point in free space by a current passing through the loop of a coil is identical to the

magnetic field produced in the loop if that current source were placed at that point in free space. A result of the reciprocity theorem is thus an antenna (or RF coil) is equally effective in transmission as it is in reception, and therefore, the B_1^+ transmit and B_1^- receive of the coil is the same.

Near and far field characteristics of coils

The electric and magnetic fields produced by an RF coil exists in three distinct regions: the reactive near field, Fresnel – radiating near field, or transition zone, and the Fraunhofer far field. A careful differentiation of these regions must be present in the analysis of RF coils. In standard MR imaging, RF coils operate in the near field. The near field is defined as the region where the wavelength of RF signal is long relative to the imaging sample ($d \leq 0.62\sqrt{D_{antenna}^3/\lambda}$). Here, the E and H fields are out of phase by 90° . The short distance between coil and sample thus allows for analysis of generated electromagnetic fields in the sample via the electric and magnetic vector potentials. This is in contrast to the far field ($d \geq 2D_{antenna}^2/\lambda$) where the electromagnetic waves of the signal are self-sustaining and propagate freely. The E and H fields are in-phase, orthogonal to each other, and radiate in the direction of propagation. The region is far enough away such that analysis can be performed by treating the antenna as a point source. Within the near field, magnetic field strength decreases by $1/r^3$ and electric field strength by $1/r^2$, while it is $1/r$ for both fields in the far field region. Between the near field and far field – the Fresnel region ($0.62\sqrt{D_{antenna}^3/\lambda} \leq d \leq 2D_{antenna}^2/\lambda$) – radiating fields begin to emerge but the shape of the radiation pattern varies significantly with distance as they are still affected by reactive fields.

Interfacing RF coils to MRI hardware

The resonant frequency of any coil must be tuned to the Larmor frequency of the nucleus of interest. The resonance of an LC circuit modelling a coil is:

$$f = \frac{1}{2\pi\sqrt{LC}}$$

To connect a coil to the MRI, the impedance of the coil must be matched to 50 Ω . This 50 Ω is a standardized value for many radiofrequency systems. The matching of coils and system hardware to this system impedance reduces the reflection of input power at the interface between the coil and the MRI scanner hardware. The figure 2.1 depicts an L-network formed by C_{tune} and C_{match} used to match the coil. L-networks may be composed from inductors, capacitors, and resistors. In MRI coil applications, inductors and capacitors are exclusively used as the use of resistors can lead to significant heat dissipation. There are various other methods to tune and match coils to the system impedance: microstrip tuning stubs may be used but they apply only specifically to coils fabricated on a printed circuit board. L-networks provide the most robust and compatible way to interface arbitrary coils to the MRI hardware (Fujita et al. 2013).

2.3 Fractal antennas

Antennas in radiofrequency engineering consist of a wide variety of designs trading off physical size, material cost, propagation characteristics, and other performance considerations. Antenna designs may vary from quarter-wavelength monopoles and half-wavelength dipoles formed from coaxial cable (*ARRL Antenna Book 2019*), to planar

patch antennas laid out on printed circuit boards (Balanis 2016). In the MRI application, the RF surface coil is more properly analyzed as a small loop antenna (Gruber et al. 2018). Small loop antennas, as the name implies, are antennas formed from wire loops in circular, triangular, square, or elliptical shapes (Stutzman and Thiele 2012). The small loop antenna is preferred in receive applications as a magnetic field probe as their small size allows for local measurements over a region of interest – precisely the use case of an MRI surface coil. The small loop additionally has a low electrical resistance and is close to being purely inductive, leading to a circuit that has a high quality factor (Q). The high quality factor means that the coil will be easily tuned to become resonant at one frequency with a sharp and narrow bandwidth, effectively acting as a bandpass filter and only detecting the signals from the resonances of the nuclei of interest.

As discussed previously, the magnetic field radiation pattern of the loop is strongest closer to the conductive structures of loop (Vaidya et al. 2016). The toroidal shape of the B_1^+ field has a weaker “null zone” in the central region of the loop, with a stronger field immediately above the conductive loop. Research into reducing the inhomogeneity in this field is of great interest.

Fractal shapes – shapes with self-similarity when viewed at multiple scales – are a modern innovation in antenna designs that seeks to improve antenna performance. Fractal antennas can fit physically larger antennas into smaller areas due to their unique geometry. For example, the first published analysis and design of a fractal antenna miniaturized a quarter-wavelength quad antenna to one with a fractal-shaped quad antenna with a side length of one-tenth the wavelength (Cohen 1995). The meandering segment lengths of the quad fractal antenna allows for the properties of the

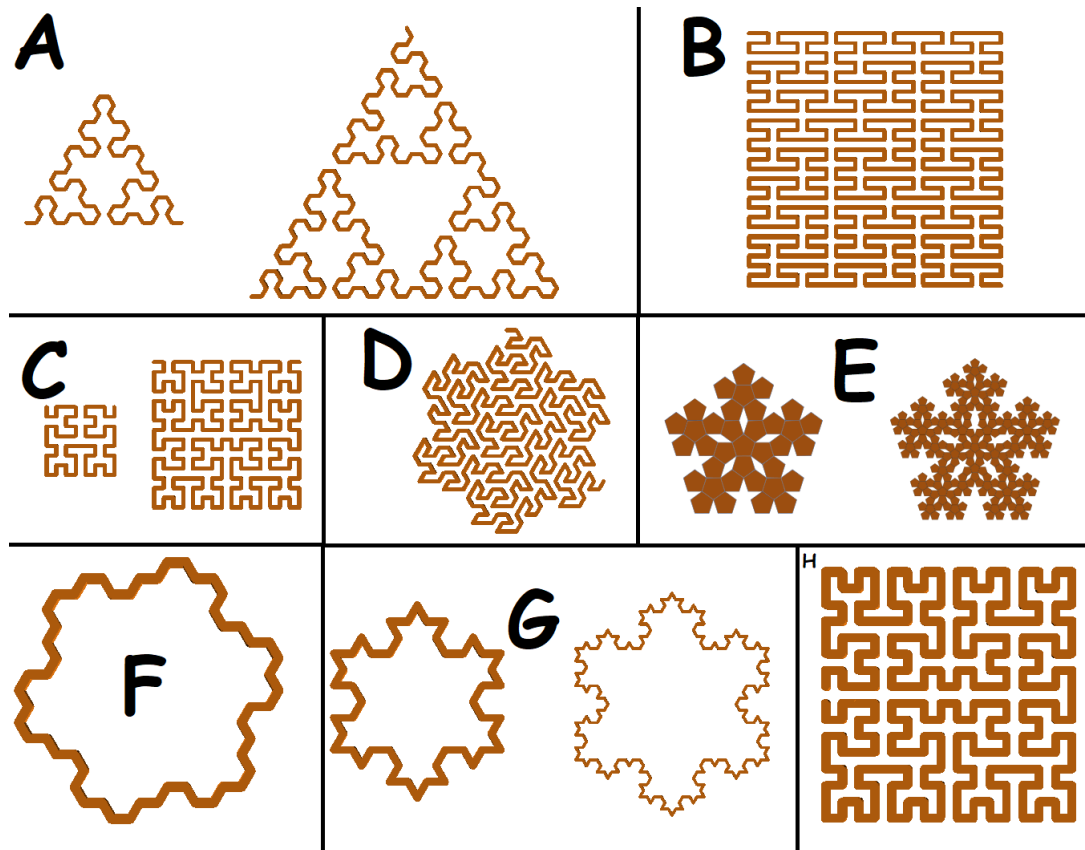


FIGURE 2.2: Fractals - A: Sierpinski arrowhead, levels 2, 3; B: Peano curve; C: Hilbert curve, levels 4, 5; D: Gosper arrowhead; E: n-flake “pentaflake”, levels 2, 3; F: Gosper island curve; G: Koch snowflake, levels 2, 3; H: Moore curve

larger quad reference antenna to be compressed into a smaller size. Additionally, the current path of a fractal antenna is longer and thus allows more flexibility when performing impedance matching.

Fractals can be parameterized by their *level* or *order*, which describes the iteration depth of the generation algorithm used to define the fractal. Figure 2.2 depicts the wide variety of fractal shapes, some with multiple iteration depths for the algorithm used to generate the fractal. All of the depicted fractals (sans n-flake) in figure 2.2 are fractals that can be generated using a rewriting system known as an L-system or

Lindenmayer system. L-systems describe a mathematical formal grammar where an alphabet of symbols, initial “axiom”, and set of rules can be used to generate a string of symbols. In a simple example of an alphabet of characters **A** and **B**, a set of rules of $\{\mathbf{A} \rightarrow \mathbf{AB}, \mathbf{B} \rightarrow \mathbf{A}\}$, and an axiom of **A**, the first iterations are thus:

$$\begin{aligned}n = 0 : & \mathbf{A} \\n = 1 : & \mathbf{AB} \\n = 2 : & \mathbf{ABA} \\n = 3 : & \mathbf{ABAAB}\end{aligned}\tag{2.17}$$

In the first iteration ($n = 1$), the symbol **A** from the axiom is rewritten into **AB** following the first rule in the rule set. In the second iteration ($n = 2$), the symbol **A** is rewritten as before, and then the symbol **B** is rewritten into **A**. This rewriting continues until the number of iterations reaches a specified stop point.

In the generation of fractals, a single linear segment serves as the axiom and at each recursive iteration of the rewrite rules, the linear segment is replaced by segments with different lengths and angles. In the Sierpinski fractal of figure 2.2, the L-system consists of: alphabet: **A B**; constants: + -; axiom: **A**; rules: $\{\mathbf{A} \rightarrow \mathbf{B - A - B}, \mathbf{B} \rightarrow \mathbf{A+B+A}\}$. In generating the fractal, the symbols are interpreted as “turtle graphics” as a cursor on a Cartesian plane. **A** and **B** mean “draw a line segment”, + means “turn left by an angle of 60°”, and - means “turn right by angle of 60°”. Thus, a fractal can easily be generated by using the L-system rewriting rules.

First used in antenna designs in the 1990s, fractals were used in order to shrink the physical dimensions of a quad antenna while maintaining the same radiation pattern

and performance characteristics (Cohen 1995). Fractal antennas have since been expanded into other use cases within radiofrequency engineering. The most similar use case to surface coils in MRI is that of the ultra high frequency (UHF) radiofrequency identification devices (RFID) in remote keyless entry systems. Like in MRI applications, reducing the null zone and ensuring a uniform magnetic field distribution are key priorities in an RFID system. Koch-shaped fractal loop antennas have been shown to perform satisfactorily in research environments using planar PCB-based (Tao et al. 2017) and in wire loop structures (Pakkathillam et al. 2013). However, these fractal-shaped antennas are designed to work at UHF frequencies – in this case 915 MHz – higher than the frequencies required for nuclei in 3T as depicted in table 2.1.

In the MRI field, relatively little research has been performed in adapting the use of fractal geometry to RF coils. A patent claims that a Koch-shaped fractal can have higher signal-to-noise ratio as well as more uniform magnetic field radiation pattern for ^1H in 3T and 7T systems (Ha et al. 2014). Research into adapting Koch-shaped fractal loops for use in ^{129}Xe imaging shows that the performance benefits are still achievable (Lemus et al. 2018). Of all the fractal research in both MRI coils and RFID systems, only Koch-shape geometries have been considered. Further research into different fractal shapes should be emphasized.

Chapter 3

Design Methodology and Simulations

In this chapter, the design methodology for the fractal geometry coils is outlined. The goal is to design and investigate fractal-shaped geometry surface coils, which are hypothesized to have improved B_1^+ transmit field homogeneity and have better signal-to-noise ratio compared to traditional surface coil designs. Each design requirement is explained in detail and their potential effect on coil performance discussed.

The two questions this thesis seeks to answer are:

1. Do fractal coils produce a stronger magnetic field than that of a reference coil within a specific region of interest?
2. Do fractal coils produce a more uniform magnetic field than that of a reference coil within a specific region of interest?

3.1 Design Methods, Materials and Methodology

This section describes the general overview for the design, fabrication and testing of an RF coil.

RF surface coils for MR imaging can be constructed via a variety of methods. Bent or shaped wire loops (Morey et al. 2015), copper tape adhered to acrylic (Yan et al. 2018), stitched conductive thread in fabric (Vincent and Rispoli 2019), screen printing (Corea et al. 2017), and etched printed circuit boards (PCB) are methods in which surface coils are constructed. In this thesis, the decision was taken to construct the fractal-geometry coils and reference coil using traditional printed circuit boards. The use of printed circuit boards allows for precise and accurately laid-out copper traces. This is essential in ensuring that the fractal structure of the coils is not only maintained on one coil, but consistent between production batches.

The workflow for designing an RF coil is depicted in Figure 3.1. The workflow can be summarized into the following:

1. Construct fractal geometry using OpenSCAD (Kinel and Wolf 2019) or Fusion360 (Autodesk 2020), using KiCad (Charras 2020) to fabricate the coils
2. Simulate the coils in HFSS (Ansys HFSS R19.2 2018) to evaluate the B_1^\pm magnetic field
3. Fabricate the coils
4. Tune and match coil to 50Ω , providing an acceptable return loss for performance
5. Compare results between simulated and constructed coils

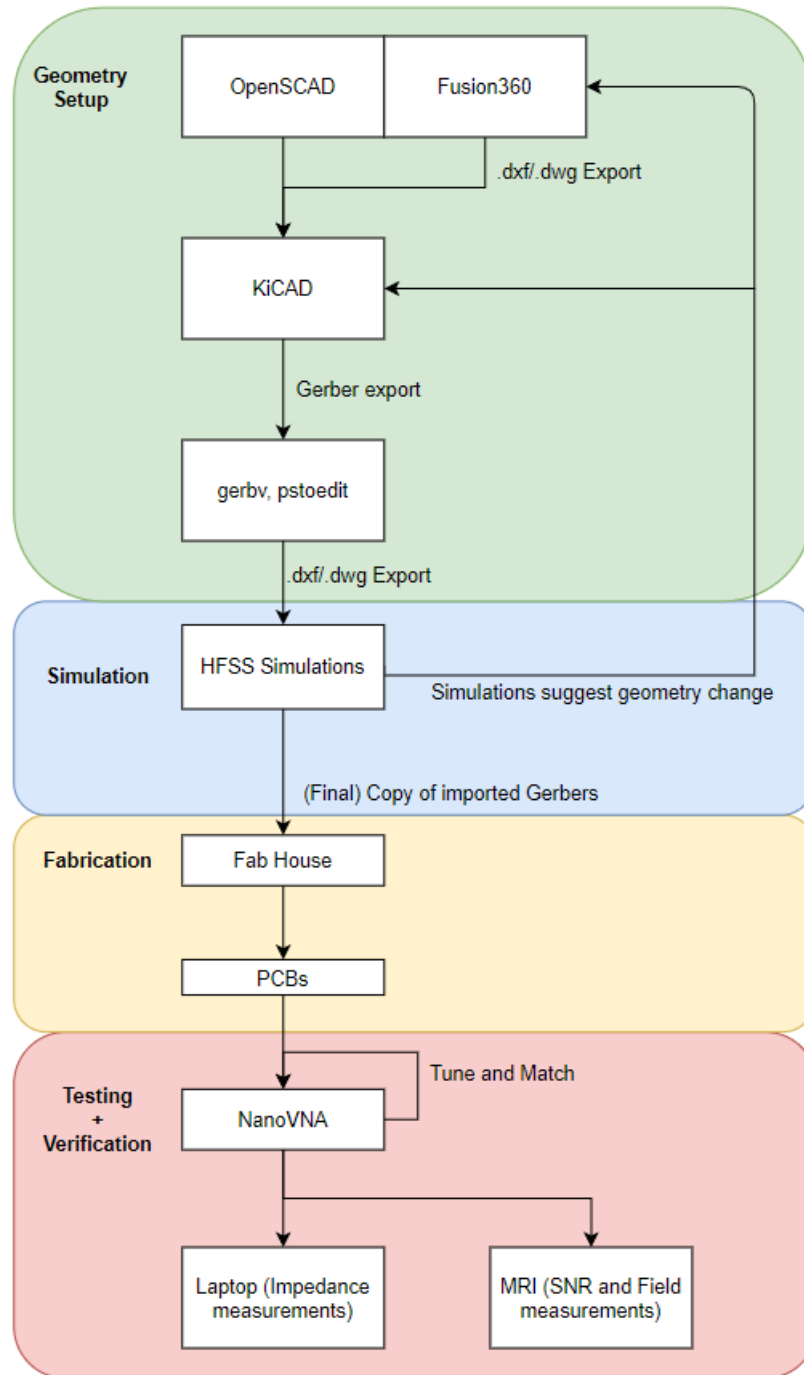


FIGURE 3.1: RF coil design methodology workflow

The fractal geometry – once selected – is modeled in OpenSCAD for fractals that can be generated by an algorithm and in Fusion360 otherwise. The use of KiCad ensures that the representation of the fractal coil is preserved between the simulation software and constructed coils.

3.1.1 Fractal design selection

As discussed in chapter 2, fractal designs exist in a variety of shapes and iteration depths. The particular effects of each fractal shape and depth in the context of magnetic resonance imaging is insufficiently researched and provides an avenue of exploration for this work.

It is shown that a Koch-style fractal shape RF coil (Lemus et al. 2018) or antenna (Tao et al. 2017) leads to a more uniform B_1^\pm magnetic field. The uniformity of the field is hypothesized to be caused by an increase in corner-bent segments as compared to a traditional circular coil. These corner bends can lead to a more even coverage of the planar region – called a “space-filling” curve – leading to a more uniform field within the planar region. Segmenting the loop into multiple, short segments can also lead to an increase in magnetic field strength (Pakkathillam et al. 2013; Zhurbenko 2016).

The fractal designs chosen were selected based on their space-filling shape and number of corner bends. Fractal designs with an extreme number of corner bends (Peano, Hilbert curves) were rejected as they would require a significant number of in-line capacitors for tuning and in order to break up the electric field. Additionally, the shorter segment lengths between each corner bend may not allow each copper track segment to resonate as the lengths are far shorter than the wavelengths of the 35.3 MHz signal from the ^{129}Xe resonance. Some fractals (Gosper arrowhead, Hilbert curves) were

rejected due to their endpoints being located too far away from each other to allow a connection using a PCB-mounted SMA jack, or soldered-on coaxial cable. Fractal curves with near-annular shapes as opposed to planar fractal carpets were chosen as their annular shape resembled traditional RF coils and those found in the literature. The space-filling properties of these fractals allows for an analysis and confirmation into the effect of B_1^+ field uniformity. The fractal depth of each coil was chosen to maintain the near-annular shape, as well as preventing each segment from becoming too short. In particular, each fractal was chosen as such (see appendix [A](#) for OpenSCAD scripts used in rule rewriting):

1. Gosper island fractal, level 3 - Figure [3.2](#)

- generated using L-system
- most similar shape to circular coil, with same radius
- uses six capacitors for tuning as well as to break up electric field

2. Pentaflake “snowflake” fractal, level 2 - Figure [3.3](#)

- manually drawn in Fusion360 as it was not an L-system fractal
- uses five capacitors for tuning
- pentagon geometric shape provides the best plane-filling compared to the other fractal coils

3. Sierpinski arrowhead fractal, level 4 - Figure [3.4](#)

- generated using L-system

- most distinct from circular coil, with same longitudinal distance between feed point and third tuning capacitor as the radius of the circular coil
- the effect of having the closely-spaced tracks in the center of the coil is unknown

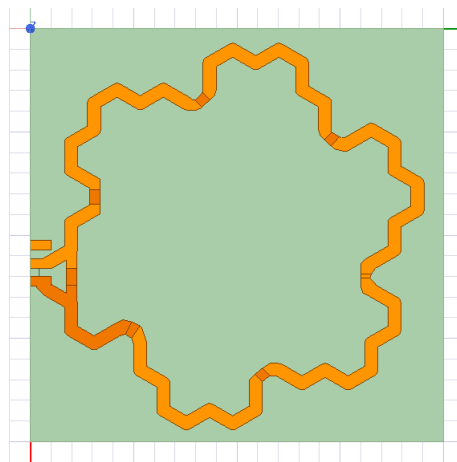


FIGURE 3.2: Gosper island fractal, level 3

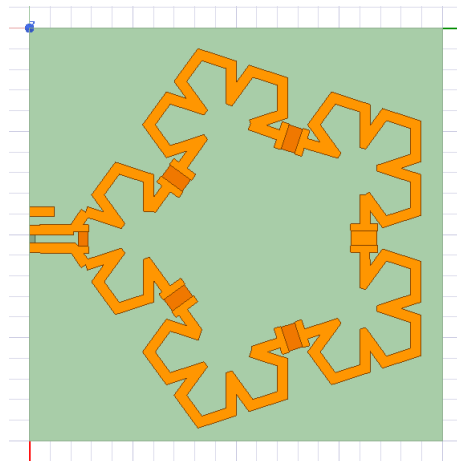


FIGURE 3.3: n-flake “pentaflake” fractal, level 2

In addition to the three fractal coils, a standard circular coil (Figure 3.5) must be designed and tested. The circular coil will provide a reference to which the fractal coils will be compared.

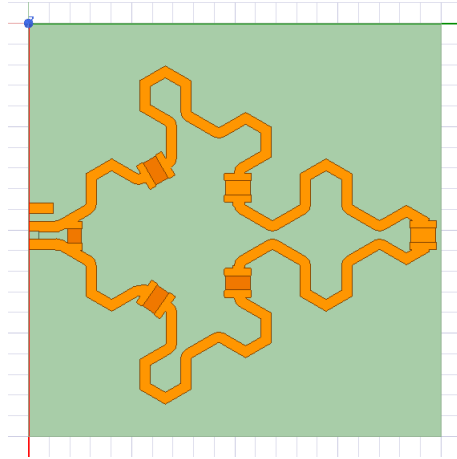


FIGURE 3.4: Sierpinski arrowhead fractal, level 4

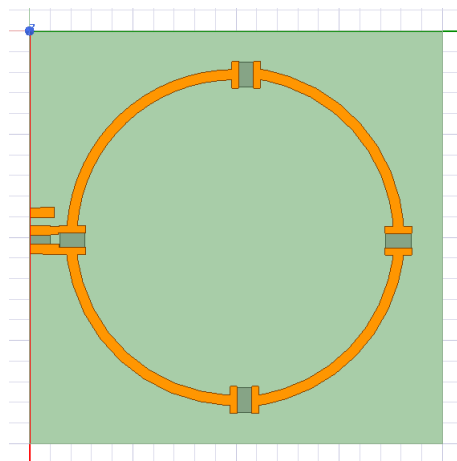


FIGURE 3.5: Reference coil

3.2 Simulations

After the initial selection of fractal designs, software electromagnetic simulation of the coil was performed. Simulation although not required, allows for cursory insights before further design steps are taken. The simulation software can provide detailed information about the emitted electric and magnetic fields due to an induced stimulus on the coil, surface currents along the copper trace of the coil, and impedance parameters for matching the RF coil to the system characteristic impedance.

Simulations of preliminary fractal coil designs were performed in Ansys HFSS Ansys HFSS R19.2 [2018](#).

The simulations of the fractal coils follows standard design guidelines and practices. The dielectric substrate (FR4, Tg 130 (glass transition temperature), dielectric constant $\epsilon_r = 4.35$), external PCB dimensions (10 cm \times 10 cm), dielectric thickness (1.6 mm), copper thickness (1 oz. per square foot, $\approx 35\mu\text{m}$), and trace width (2.5 mm) were all identical between the coils. The only differences between the coils were copper trace path, which traced a fractal shape or circle in the case of the reference coil. Additionally, the reference coil had three evenly-spaced tuning capacitors, while the fractal coils had five in the case of the Sierpinski and pentaflake coil, and six in the Gosper coil. The number of capacitors affects the electric and magnetic field emitted by the coil, as hypothesized and tested in (Dobkin et al. [2007](#)). In particular, the splitting of the tuning capacitors into multiple capacitors physically breaks up the loop into short segments. These short segments cause the entire loop to behave as a small loop antenna, which will then enable a constant current distribution and thus allow the generation of strong near-field magnetic fields. Additionally, using multiple capacitors reduces the specification of individual higher-voltage rated capacitors as the electric field is now distributed across multiple capacitors.

For the layout of the geometry within the simulation software, a 100 mm by 100 mm by 1.6 mm substrate was created with a 35 μm track of copper placed on top. In the earlier analysis by Lemus et al. (Lemus et al. [2018](#)), the copper traces were simulated on top of a ground plane of copper placed on the opposite side of the substrate. The design by Lemus et al. simulates that of a patch antenna while the design in this

thesis simulates that of a loop antenna. A patch antenna is an antenna that uses a copper trace above a ground plane. The copper trace above a ground plane forms what is known as a microstrip transmission line and thus the patch antenna is also referred to as a microstrip antenna. The microstrip transmission line serves as the radiating element in combination with the ground plane located underneath. The fringing electric fields near the edges of the copper trace lead to the creation of the radiated electric field. In contrast, a small loop antenna (as discussed previously in chapter 2) is an antenna that couples to the magnetic field in the region close to the antenna. Given that loop antennas are the standard antenna geometry used for the design and construction MRI coils, the use of the ground plane on the bottom surface of the substrate was not included.

3.2.1 Metrics for Tuning, Matching and Field Measurements

Proper tuning of the RF coils to 50Ω is essential in ensuring that the field generated by the coils in simulation are fairly compared. A mismatch between the coil impedance and lumped port impedance would lead to a reduced amount of power supplied to the coil, adversely affecting simulation results. After laying out the copper traces in Ansys HFSS, the capacitors were added as lumped elements.

In order to determine the value of capacitors for matching and tuning, the values of the tuning capacitor (C_{tune}) and matching capacitors (C_{match}) were varied using a parametric search and the coil simulated with an excitation of 35.3 MHz – the Larmor frequency of ^{129}Xe . The metric used to determine how closely two systems are matched is via the *reflection coefficient*, written as $|S_{11}|$ or Γ . The reflection coefficient describes the magnitude of reflected signal at the input port of a system. In

this case, reflection coefficient is the magnitude of input power to reflected power, $\Gamma = 10 \log_{10}(P_{reflected}/P_{input})$, in dB. An acceptable maximum for the return loss of a well-matched RF coil is less than -6 dB (Sohn et al. 2014) to -20 dB (Fujita et al. 2013). A return loss of -6 dB indicates a reflection of about 25% of the input power, while a return loss of -10 dB indicates approximately 10% reflection. With -15 dB return loss, 3% of the input power is reflected and with -20 dB return loss, 1%.

The RF coils will be considered matched if at the resonance frequency of 35.3 MHz the reflection coefficient is less than -15 dB.

The examination of the electric and magnetic field involves measuring the electric and magnetic fields of the coils in the xy , yz and xz slices. The mean ($\mu = \Sigma x/N$) and standard deviation ($\sigma = \sqrt{\Sigma |x - \mu|^2/N}$) for each planar slice will be compared. Comparing means and variances using statistical tests will allow for judging whether one coil produces a field that is stronger (using the signal to noise ratio) or is more uniform (using the coefficient of variations) than that of the reference coil.

To test whether one coil has a stronger signal to noise ratio, the magnetic field strength produced by each coil at each slice can be compared. The unpaired two-sample t-test can be used in order to determine if the mean field strength between the fractal coils have a statistically significant difference from that of the reference coil. From a comparison of the means, the SNR can thus be qualitatively ranked based on the magnitude of the means. A higher average magnetic field strength for a coil would lead to a higher SNR in an imaging application.

To test uniformity of the fields, a comparison of the coefficient of variations ($c_v = \sigma/\mu$) can be used. The coefficient of variations parameterizes the variability of the

data with respect to the mean, and thus can serve as a uniformity test for the coils. The F-test statistic can be used to compare the standard deviations of the fractal coils and determine if there is a statistically significant difference from that of the reference coil. The coils with a larger coefficient will thus be judged more inhomogeneous than a coil with a lower coefficient of uniformity. Tests such as the chi-squared test or Kologomorov-Smirnov test may also be used to compare the distribution of the field to an expected uniform distribution.

However, the F-test statistic to compare standard deviations and t-test statistic to compare the means cannot be used as the assumptions for their use presume that the data is normally distributed (the data is symmetric around a mean and the distribution converges to the Gaussian distribution), as well as only usable when the standard deviations are equal across samples. In the case of the electric and magnetic field simulations, there is no indication that either of the two assumptions hold true and thus alternative methods of comparing means and variances is required.

The Bartlett and Levene test are commonly used alternatives to the F-test, with the Bartlett test being more sensitive to normal distributions while the Levene test is more robust for data that is non-normal. The Bartlett and Levene tests the null hypothesis of whether the variances of the data are equal against the variances being different. A p-value of less than the significance value of 0.05 suggests that there is evidence that the variances of the data sets used in the comparison are different, and thus a comparison of means using the t-test or F-statistic is valid and can be used. Instead of the t-test or F-statistic, a quicker comparison of the SNR values using the normalized σ can be used so as long as the variances are initially confirmed distinct.

The metrics used to evaluate the field performance of each coil will be an examination of the electric and magnetic field above the surface of the coil using the statistical methods mentioned above. For the Bartlett and Levene tests, the standard significance value of $\alpha = 0.05$ was used. Additionally, the tuning of each coil using the reflection coefficient will be examined in order to ensure a fair comparison.

3.2.2 Simulation Results

Results and discussion for the simulations are available in chapter 5. The simulation results will be compared to the results obtained by experimental procedure and discussed.

Chapter 4

Fabrication and Experimental Procedure

This chapter discusses the fabrication of the fractal and reference RF coils. Particular details in material, component selection and fabrication technique for each coil are discussed. The experimental procedure for tuning and matching the coils using a vector network analyzer is outlined.

4.1 Fabrication

Following the acceptable simulation of the RF coils, the fabrication procedure can begin. To maintain the most reliable and accurate results, the fabricated coils must maintain as many similarities between the simulation parameters and the PCB parameters.

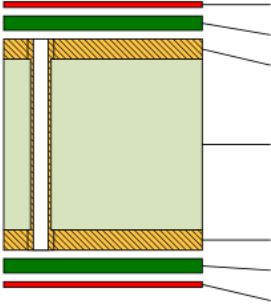
In the previous chapter, the parameters of the PCB used in the simulations of the RF coils were:

- dielectric substrate – FR4, Tg 130 (glass transition temperature), dielectric constant $\epsilon_r = 4.35$, loss tangent $\tan(\delta) = 0.02$
- PCB dimensions – 10 cm \times 10 cm
- dielectric thickness – 1.6 mm
- copper thickness – 1 oz. per square foot ($\approx 34.8 \mu\text{m}$)
- copper trace width – 2.5 mm

The dielectric substrate parameter describes the non-conductive backing material on which the copper traces are laminated. FR4 is an industry standard substrate material created from woven sheets of fibreglass laminated with epoxy. The FR4 has a dielectric constant or relative permittivity (ϵ_r) of 4.35. The dielectric constant describes the reduction of the electric field strength within the material relative to vacuum. Therefore the value of the relative permittivity of the vacuum is 1. FR4 is the most widely used substrate, but there are specialty substrates for use in specialized applications. Aluminum core substrates are often used in high-power applications such as motor drivers, while the high-frequency demands of microwave RF printed circuit boards require materials with lower dielectric constants. Figure 4.1 depicts the layer stackup of the PCB of each RF coil.

As an approximation, the B_1^+ region of an RF coil extends to a depth equal to that of the radius of the loop. Most RF surface coils are on the order of 10 cm, and thus that value was chosen as the PCB dimension. The cost to manufacture a printed circuit board from most fabrication services is inexpensive ($< \$10$) below a 10 cm square and thus provides additional motivation for restricting the size.

Layer Stack Legend



Material	Layer	Thickness	Dielectric Material	Type	Gerber
	Top Overlay			Legend	GTO
Surface Material	Top Solder	0.03mm	SM-001	Solder Mask	GTS
Copper	TOP	0.04mm		Signal	GTL
Core		1.52mm	FR-4	Dielectric	
Copper	BOTTOM	0.04mm		Signal	GBL
Surface Material	Bottom Solder	0.03mm	SM-001	Solder Mask	GBS
	Bottom Overlay			Legend	GBO
Total thickness: 1.65mm					

FIGURE 4.1: PCB layer stackup. Silkscreen overlay (top and bottom) are produced using non-conductive UV-cured epoxy ink.

The thickness of the dielectric substrate within a PCB and the thickness of the copper laminate are standardized to a set of common values for most fabrication services. A 1.6 mm substrate thickness with 1 ounce per square foot copper is the default option for most, and was chosen as it has relatively little bearing on the performance of the RF coil. The dielectric substrate thickness and copper thickness are primarily parameters used in determining the impedance of copper traces for microstrip transmission lines. Microstrip transmission lines are usually used in RF applications to interface 50-Ω surface-mount devices on a printed circuit board. The fractal RF coils do not use these devices and therefore their effect on coil performance is minimal.

The trace width of a copper track mainly affects its ability to carry current. The GE MR750 MRI system used for testing the RF coils has an output power of 8 kW (GE Healthcare 2020), which then defines the minimum trace width to be approximately 2 mm. The final trace width of 2.5 mm is up-rated to prevent any issues with heat dissipation.

Tuning and Matching

The fractal coils were tuned matched using ceramic capacitors. ATC 100B capacitors (AVX Corporation 2020) and Vishay VJ HIFREQ (Vishay Intertechnology Incorporated 2020) capacitors were used, as they are specifically designed to be compatible in a high magnetic-field environment, and they are designed for the high-voltage applications required in MRI systems. The 8 kW output amplifier within the MRI can produce a voltage of up to 630 V and thus the capacitors are rated to 1200 V (GE Healthcare 2020). The significant over-rating of the voltage specifications on a capacitor is a standard engineering practice as the capacitance of a capacitor is significantly decreased as the applied voltage approaches the maximum voltage specification. Capacitors are usually derated by 50% of their nominal specifications and thus the 1200 V rating of the capacitors is essential.

Recall that an L-network is used to match the RF coil to the system impedance of 50 Ω . L-networks can use two capacitors, C_{tune} and C_{match} in order to match the impedance of the coil to 50 Ω .

To begin the matching procedure, the inductance of the inserted device must be determined. A vector network analyzer (VNA) is a measurement instrument used to measure the impedance of a device under test (DUT). The VNA generates a radiofrequency signal and the amount of reflected power can be detected. By comparing the amount of transmitted power to reflected power, the reflection coefficient of the DUT can be determined at that frequency. The VNA will sweep the frequency to determine the reflection coefficient as a function of frequency, allowing the determination of the frequency response of a device. The impedance of a DUT can be determined from the

reflection coefficient as:

$$Z = Z_0 \left(\frac{1 + \Gamma}{1 - \Gamma} \right) \quad (4.1)$$

where Z_0 is the characteristic impedance of the system, in this case 50 Ω .

To measure inductance of the coil, the capacitor footprints for the C_{tune} capacitors are to be soldered as a short, while the C_{match} capacitor footprint left open. This will allow the VNA to measure the impedance of the entire copper trace. Figure 4.2 is a photograph of the measurement setup of the coils attached to an Agilent 4395A vector network analyzer. Figure 4.3 depicts the same, but with a nanoVNA. An online calculator can then be used to determine the match and tune capacitor (figure 4.4).

The values for the tuning and matching capacitors supplied by the online calculator are only ballpark figures. The physical capacitors used in tuning and matching have capacitance tolerance specifications from 5% to 10%, which require the addition of smaller capacitors to account for the error. Additionally, the 100B-series capacitors include axial leads, while the VJ HIFREQ capacitors do not. This may introduce stray parasitic inductance and capacitance that will affect the tuning of the coil to the resonance frequency as well as the matching to an acceptable reflection coefficient.

Figure 4.5 depicts the constructed RF coils with tuning and matching capacitors.

To connect the coils to the MRI scanner, SMA edge-mount connectors were originally used. However, these connectors were found to possess ferromagnetic material and as such were unsuitable for use in the MRI. Instead, 50- Ω RG-223/U coaxial cable



FIGURE 4.2: Image of impedance measurement setup using the Agilent 4395A

(a non-ferromagnetic coaxial cable) was soldered directly to the surface-mount pads previously occupied by the SMA connector.

4.2 MRI SNR evaluation

To experimentally validate the performance of each coil, the coils can be used in an MRI scanner to detect a sample of ^{129}Xe and from the signal, the SNR can be calculated. The SNR is defined by the square of the mean signal strength divided by the square of the standard deviation ($\text{SNR} = 10 \log_{10}(\mu^2/\sigma^2)$). The SNR provides a metric for the determination of whether fractal-shaped coils have a stronger B_1^+ field than

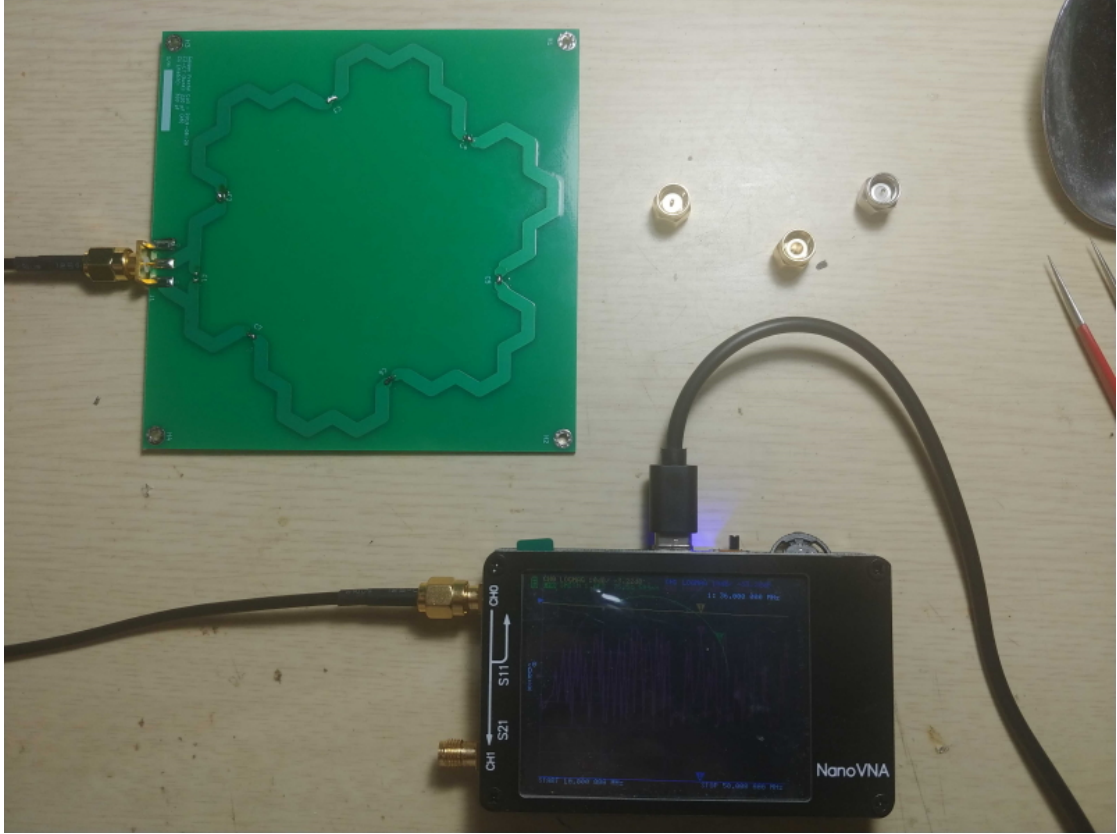


FIGURE 4.3: Image of impedance measurement setup using the nanoVNA

that of the reference coil. This is the standard SNR equation used in signal processing, although there are different equations used in different fields. In usual MRI applications, the SNR is measured using the signal and background noise standard deviation as $SNR = S_{signal}/\sigma_{Background}$, where S is the received signal amplitude, and σ is the standard deviation. Another alternative to the standard SNR equation using two signals is $SNR = \frac{S_1+S_2}{2}/\sigma_{S_1-S_2}$. For the experimental SNR measurements of the fractal and reference coils, the SNR was calculated as:

$$SNR = 10 \log_{10} \left(\frac{\mu_{Signal}^2}{\sigma_{Signal}^2} \right) \quad (4.2)$$

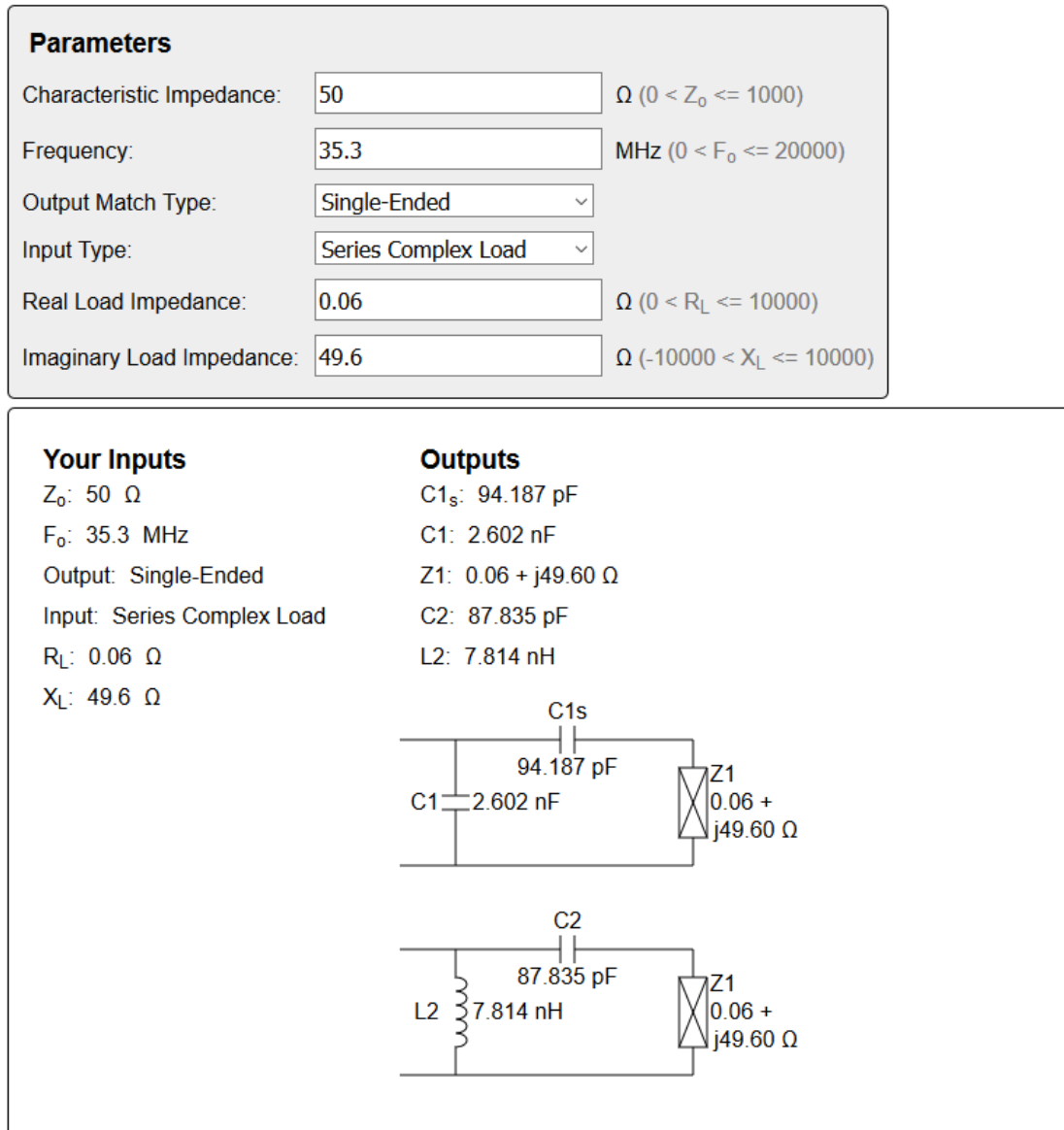


FIGURE 4.4: Image of online calculator used to achieve preliminary match (Analog Devices 2020)

where the signal acquired is the free induction decay obtained from the MRI scanner. The MRI scanner used to acquire the signal is a 3T MRI scanner at the Imaging Research Centre at St. Joseph’s Healthcare in Hamilton, Ontario (GE Healthcare 2020). A ^{129}Xe phantom (Polarean Imaging plc 2020) was used as the signal source. Additional

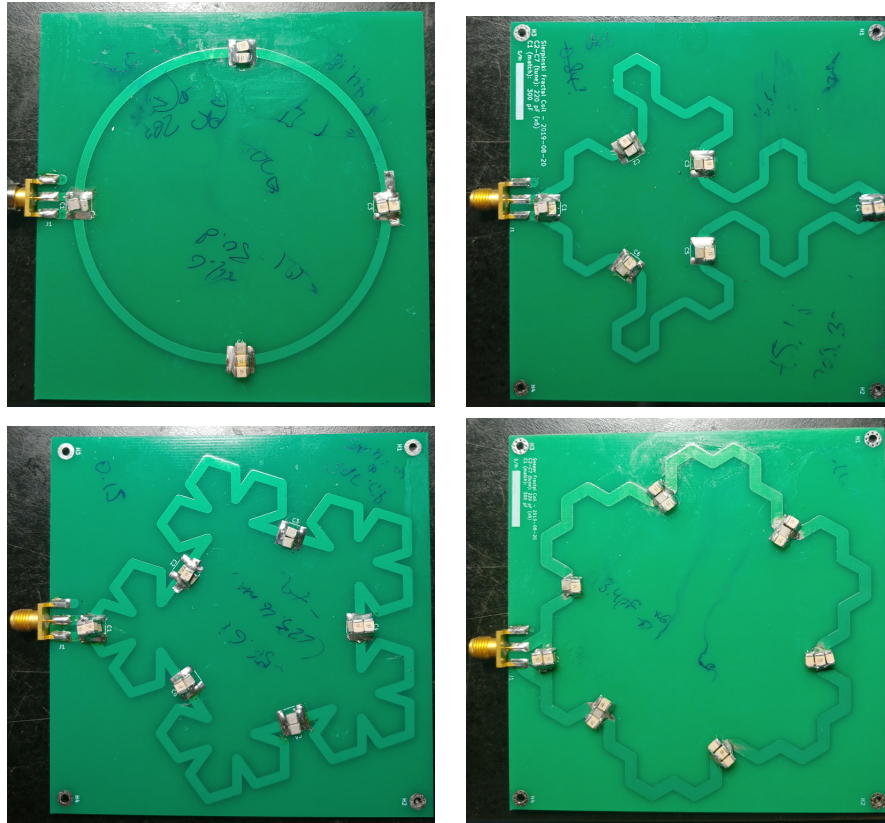


FIGURE 4.5: Images of constructed PCB coils - Top-left: Reference, top-right: Sierpinski, bottom-left: Pentaflake, bottom-right: Gosper

experimental procedure is available in chapter 5.

Bloch-Siegert pulse sequences are used to experimentally evaluate the field homogeneity of a coil in ^{129}Xe applications. The Bloch-Siegert sequence produces a phase shift in the nuclear spins after in initial excitation into the transverse plane. This phase shift is B_1^+ magnitude-dependent, and thus the inhomogeneity of the B_1^+ field is measurable by calculating the difference in phase shift across the reconstructed image (Schulte et al. 2011).

Chapter 5

Performance Evaluation

In this chapter, the results from the simulations and results from the fabrication of the coil are discussed. The electric and magnetic fields as well as reflection coefficient of each fractal coil are compared to the reference coil. The measured SNR of the RF coils provides information on whether fractal coils produce a stronger magnetic field than that of the reference coil. The field homogeneity of the coils can be experimentally evaluated by analyzing reconstructed images of scanned phantoms.

5.1 Simulation Performance Results

To allow for a fair comparison of the electric and magnetic fields in simulation, the simulated coils must first be matched to an acceptable reflection coefficient. Matching and tuning of the coils in simulation was performed and Figure 5.1 depicts the simulated reflection coefficients for each of the coils from 30 MHz to 40 MHz. Each of the coils have an acceptable reflection coefficient match of ≤ -15 dB at 35.3 MHz.

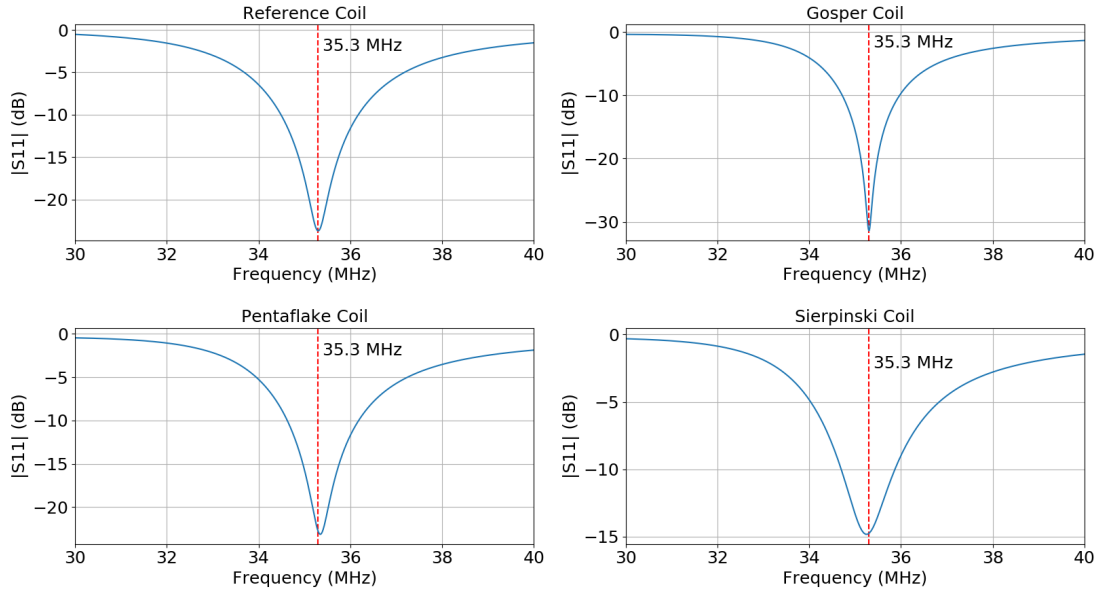


FIGURE 5.1: $|S_{11}|$ (dB) reflection coefficient measurements for simulated coils in HFSS. top-left: reference, top-right: Gosper, bottom-left: pentaflake, bottom-right: Sierpinski

5.1.1 Magnetic field analysis

The magnetic field analysis for each coil involves examining the mean, standard deviation, and coefficient of variation for the magnetic field produced by each coil. For each coil, a region of interest (ROI) must be defined for measurement purposes. Figure 5.2 depicts the regions of interest for the reference, Gosper, Sierpinski and pentaflake coils. The regions of interest were defined as the largest circular region in the center of the coil that avoids overlap with the copper traces and capacitors. The field immediately above the traces and capacitors varies significantly in magnitude and thus should be excluded from the ROI. Selecting a region that is away from the capacitors and traces thus allows for a fair comparison between the coils.

Table 5.1 shows the position and radius of each region of interest for each coil.

Coil	X position (mm)	Y position (mm)	Radius (mm)
Reference	50	50	35
Sierpinski	51	37	13
Pentaflake	52	57	22
Gosper	50	50	32

TABLE 5.1: Table of ROI dimensions for each coil

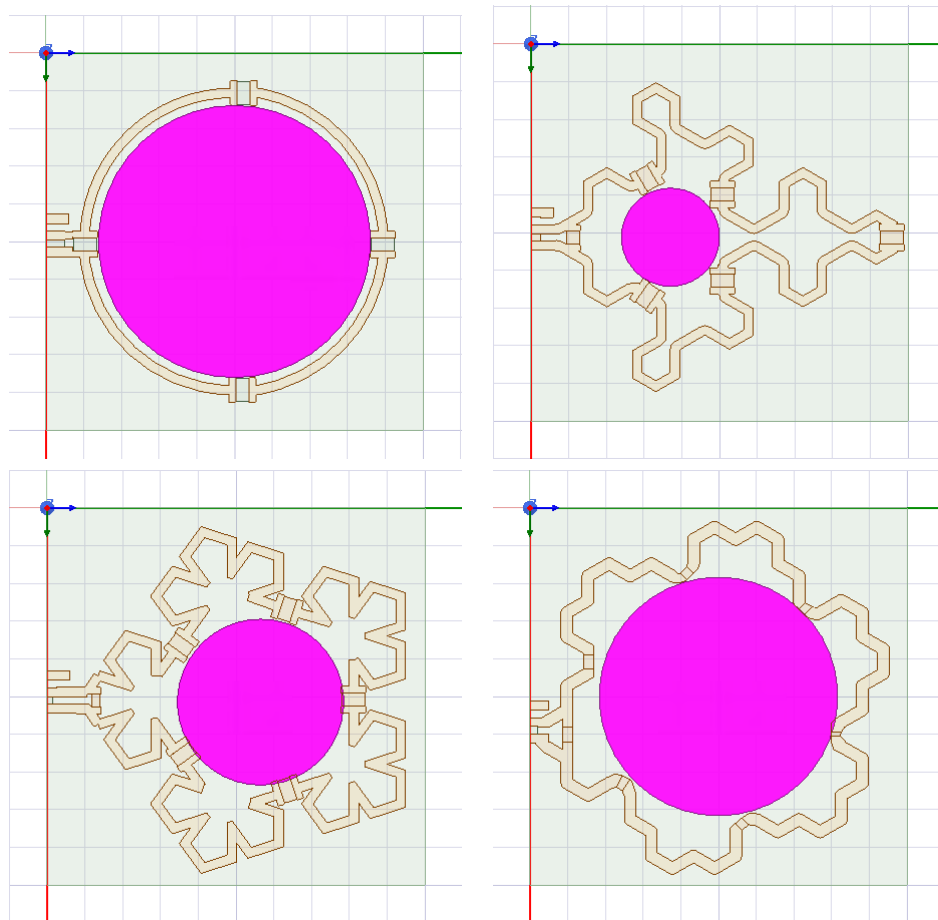


FIGURE 5.2: Image of ROI for each coil - Top-left: Reference, top-right: Sierpinski, bottom-left: pentaflake, bottom-right: Gosper

Bartlett and Levene tests

In order to compare the means and standard deviations or coefficient of variations from each of the field simulations, it is necessary to use a statistical test such as the t-test or

F-test to determine if the means or variances have a significant difference. The t-test and F-test use assumptions such as equal variances between groups, and that data in each group has a normal distribution, or else cannot be used in this analysis. Due to failure in these assumptions the alternatives – Bartlett and Levene test – were used instead. Figures 5.3 and 5.4 depict the p-value for the Bartlett and Levene test as a function of distance from the plane of the coil.

For the Bartlett and Levene tests, the sample variances for each ROI slice at a distance z from the coil were compared to the variance of the same slice of the reference coil. The null hypothesis for both tests test the assumption that variances are equal across a group of samples (i.e. $\mu_{fractal} = \mu_{reference}$). At a significance level of $\alpha = 0.05$, a p-value result less than the significance level indicates that there is evidence to suggest that the null hypothesis should be rejected and thus there is a statistical difference between the variances of the groups.

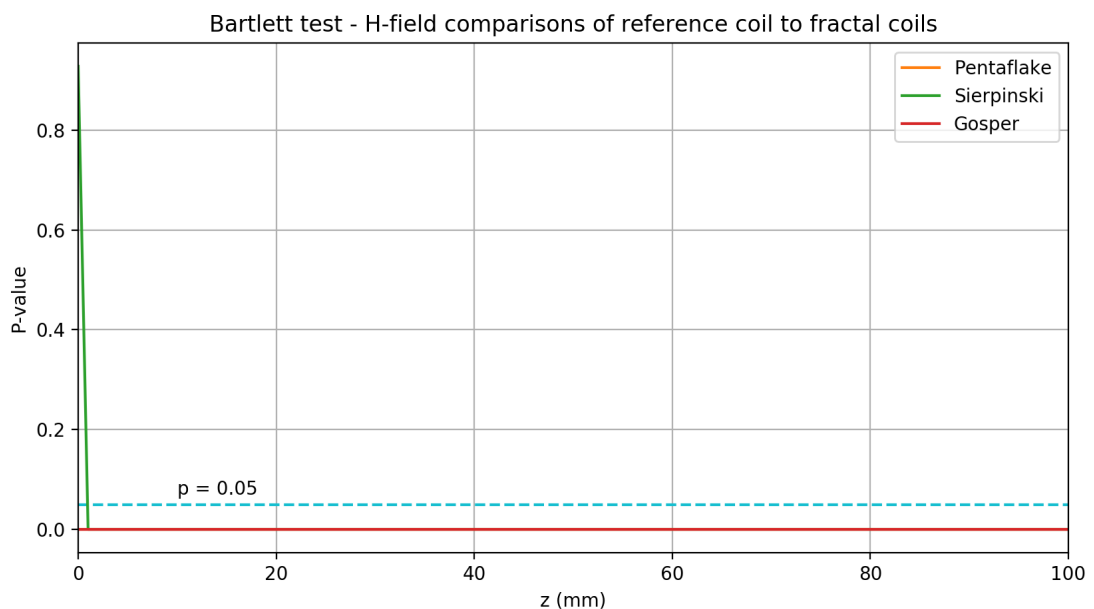


FIGURE 5.3: Bartlett test for the mean of the magnetic field, ROI slices in the z-direction

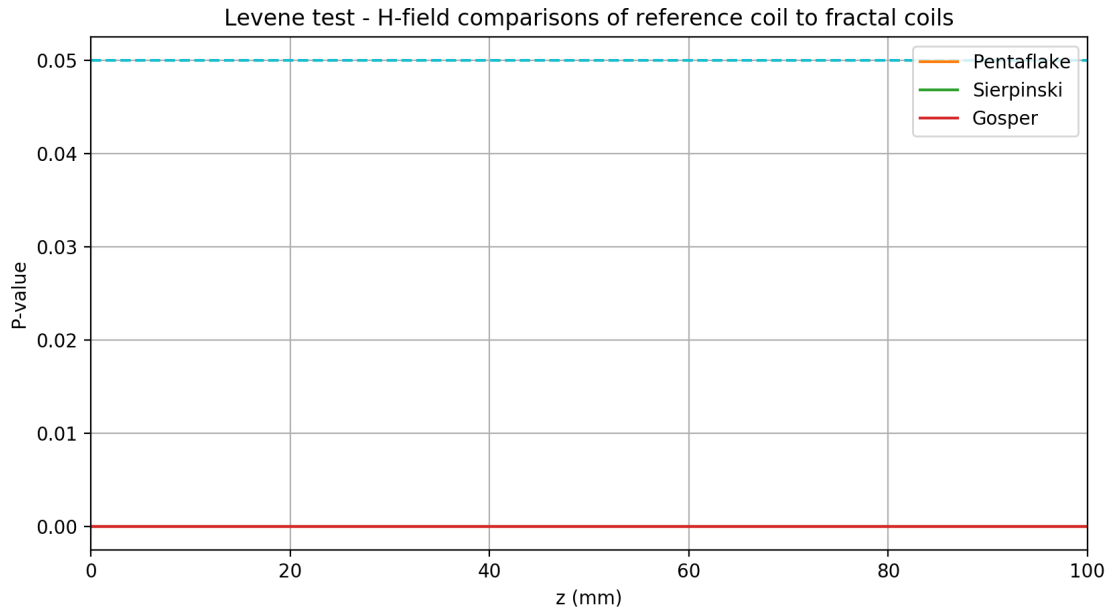


FIGURE 5.4: Levene test for the mean of the magnetic field, ROI slices in the z-direction

The Bartlett and Levene tests in figures 5.3 and 5.4 shows that variances between each coil was indeed statistically different, particularly in the regions past 1 mm. The rejection of the null hypothesis in these tests and within the regions thus allows for the direct comparison of the sample means of each coil as an indicator of B_1^\pm field strength, and thus SNR.

Magnetic field strength analysis

Figure 5.5 depicts the H field strength of each coil in the ROI planar slice from $z = 0$ to 100 mm. The standard deviation of each slice is shown as the shaded region. The mean, standard deviation, and coefficient of variations for the magnetic fields are summarized in table 5.2 for a distance of 10 mm and 20 mm from the surface of the coil. The distance chosen for the values in the table is representative of the penetration depths achieved by a coil in standard imaging applications. The surface coils used in imaging have a

penetration depth approximately equal to their radius (Gruber et al. 2018), and as such the distances were chosen to allow for a fair comparison between the coils.

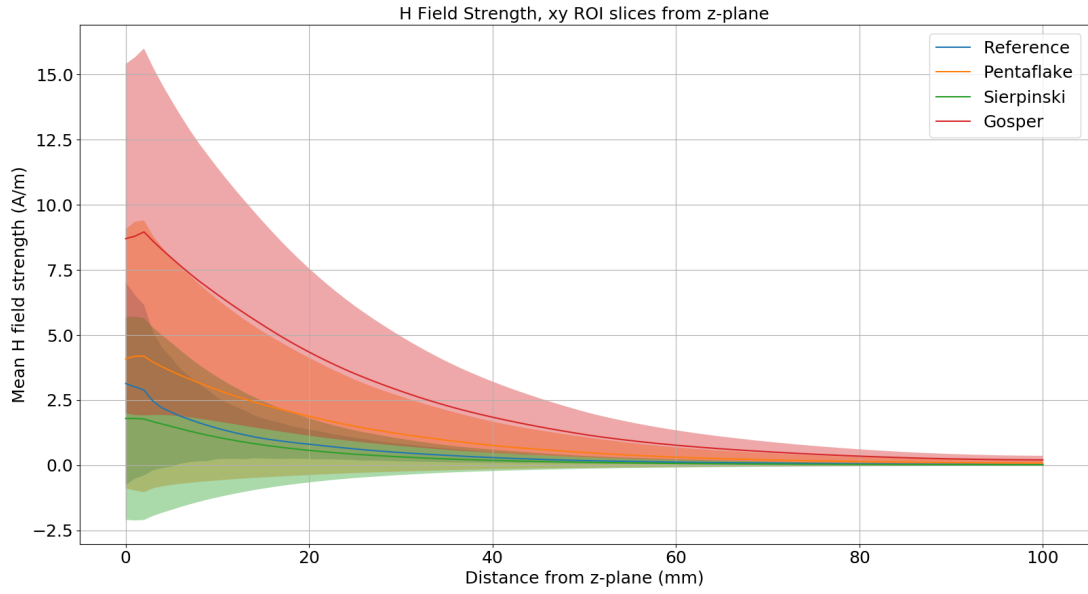


FIGURE 5.5: Simulated H-field strengths of each coil, in ROI slices in the z-plane direction

Distance (mm)	Coil	μ (A/m)	σ (A/m)	c_v
10	Reference	1.42	2.36	1.66
	Sierpinski	1.08	4.62	4.28
	Pentaflake	2.90	6.95	2.40
	Gosper	6.56	9.74	1.49
20	Reference	0.81	1.13	1.40
	Sierpinski	0.57	2.46	4.28
	Pentaflake	1.88	4.50	2.40
	Gosper	4.35	6.42	1.48

TABLE 5.2: Table of means, standard deviations and coefficients of variation for simulated H fields for fractal and reference coils at $z = 10$ mm and 20 mm

It can be seen in the above figure 5.5 and table that the means of the field strengths are larger in those of the fractal-shaped coils than that of the reference coil. The pentaflake and Gosper fractal designs had a mean field strength of 2.90 A/m and 6.56

A/m respectively, compared to that of the reference coil at a field strength of 1.42 A/m at a distance of $z = 10$ mm above the surface of the coil. At a distance of $z = 20$ mm, the mean magnetic field strength is 1.88 A/m and 4.35 A/m for the pentaflake and Gosper coils, as compared to 0.81 A/m for the reference coil.

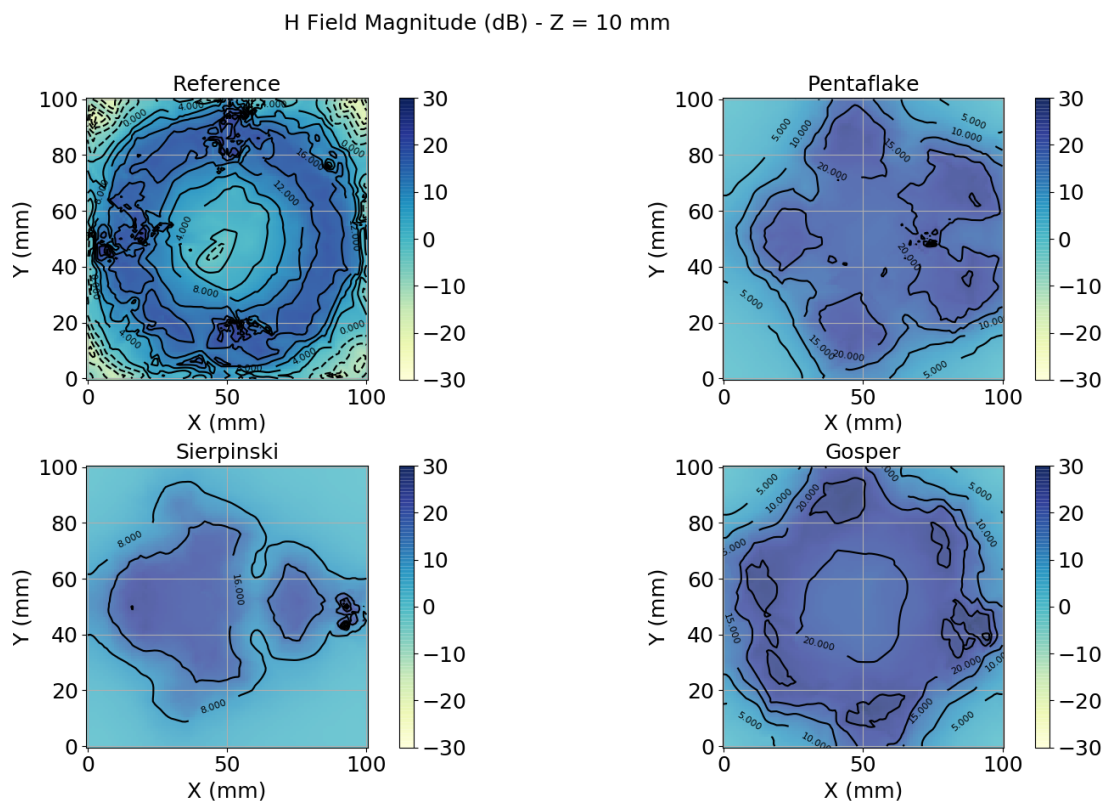


FIGURE 5.6: 2D contour plot of H field in xy plane, $z = 10$ mm

Figures 5.6 and 5.7 depict the simulated H-field for the surface coils at a distance of 10, and 20 mm respectively. The plots are color-scaled from 30 dB to -30 dB (A/m). The simulations match that of earlier research (Pakkathillam et al. 2013) and show that the field is stronger in the region near the conductive copper traces, with the “null zone” visible in the centers of the reference coil. For the fractal coils, it can be seen that there is a contour outlining 20 dB in the region of the center of the Gosper (bottom-right)

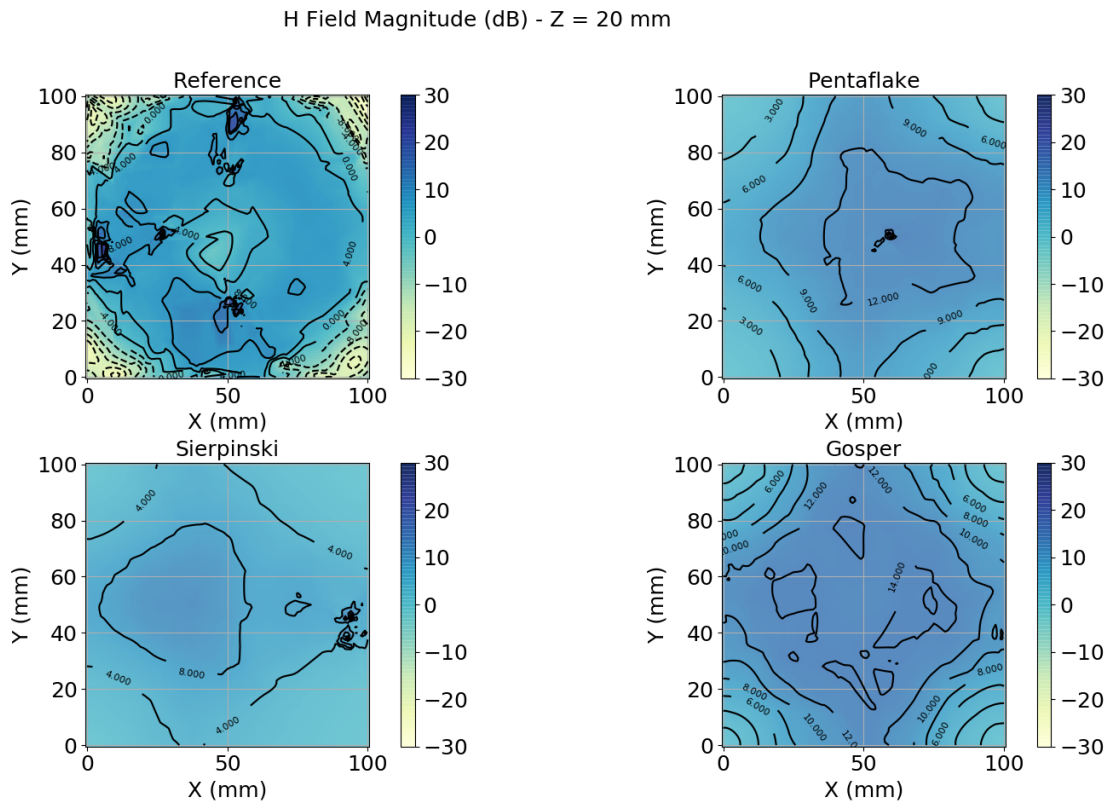


FIGURE 5.7: 2D contour plot of H field in xy plane, z = 20 mm

coil, while there is a contour of 12 dB in the region of the center of the reference coil (top-left). Similar contours can be seen in the other fractal coils, and this implies that the fields produced by the fractal coils is stronger than that of the reference coil. This can also be concluded from the mean field strength in the one-dimensional plots in figure 5.5 and table 5.2.

Field homogeneity

The figures 5.8 and 5.9 depict the magnetic field in the xz and yz planes at a distance of 50 mm. These planes intersect at center point (50mm \times 50mm) of the coils and provide information on the field in the orthogonal directions to z plots in the previous figures.

These figures provide good evidence that the magnetic field of the Gosper (bottom-right), Sierpinski (bottom-left), and pentaflake (top-right) coils are homogeneous. The -15 dB contour line can be seen extending across the x-direction in the fractal coils, but cannot be seen in the reference coil, as there is a null in the center.

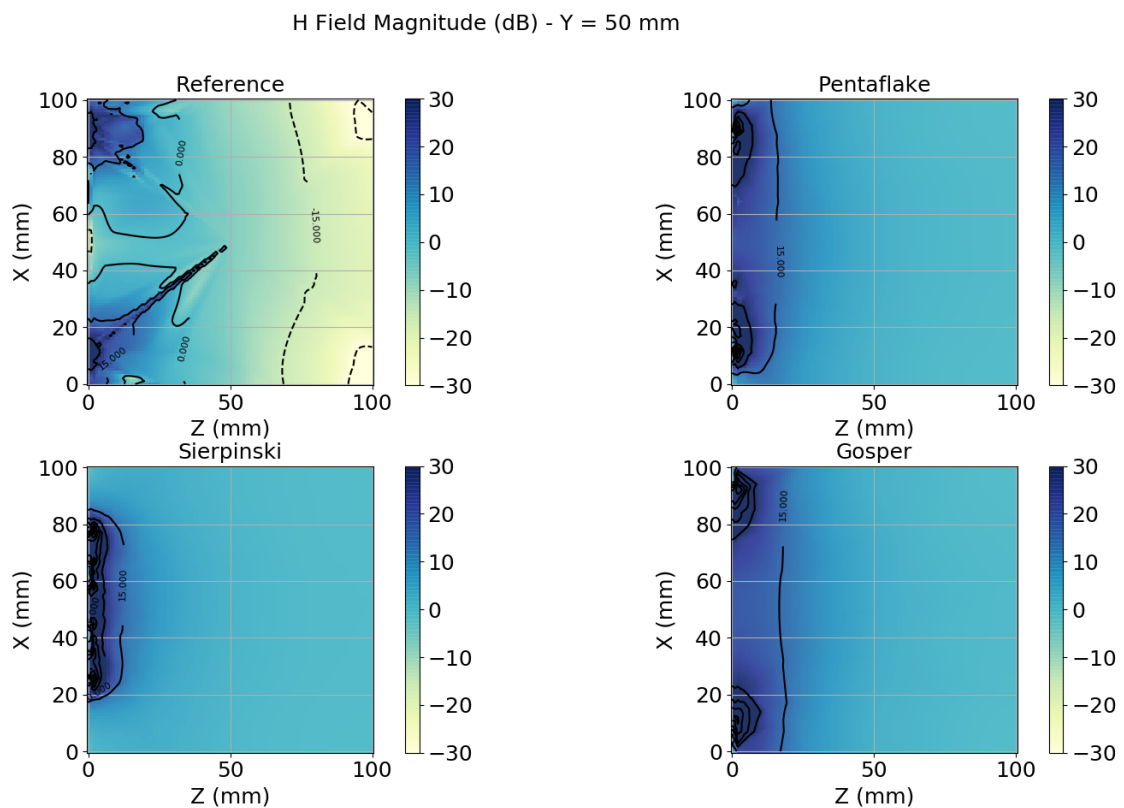


FIGURE 5.8: 2D contour plots of H field in xz plane, y = 50 mm

Although the contour plots in figures 5.6, 5.7, 5.8 and 5.9 can also be interpreted to show that that the fractal coils are more inhomogenous due to the presence of more contour lines in a region of interest than in the reference coil, table 5.2 depicts that the coefficient of variation is smaller in the Gosper fractal coil at a distance of 10 mm than that of the reference coil. This gives a numerical metric rather than relying the visual contour plots to compare field homogeneity. The interpretation of the coefficient of

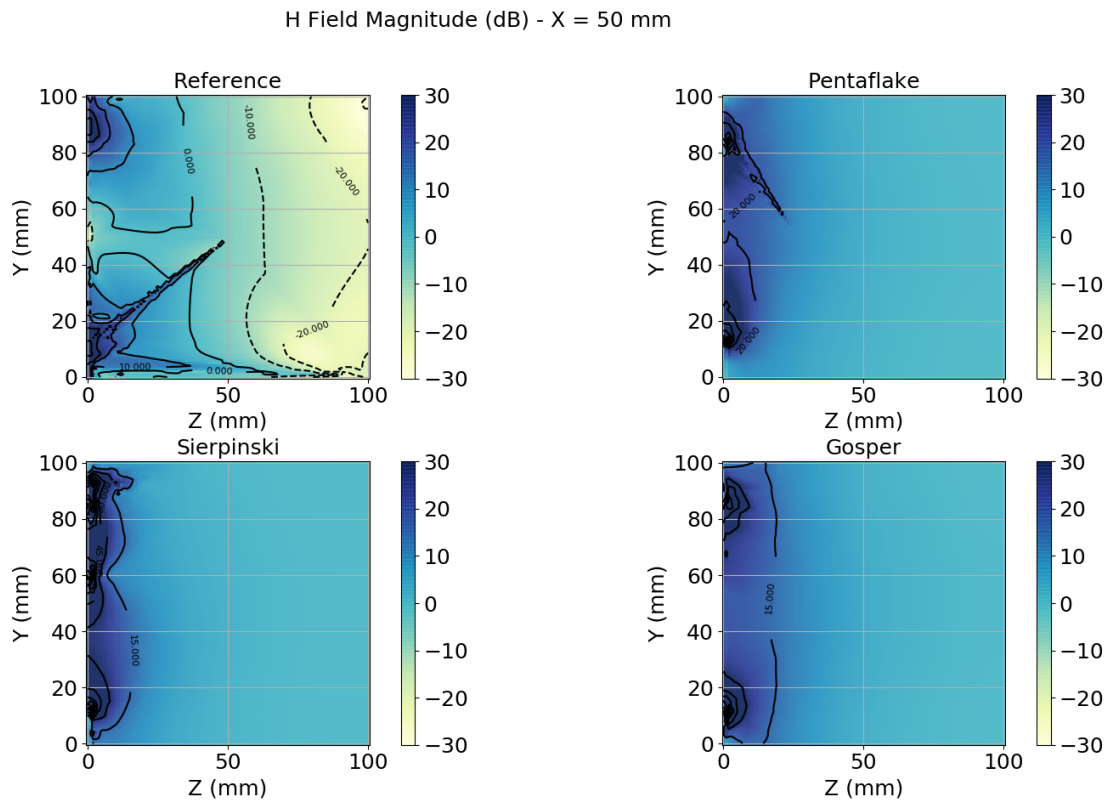


FIGURE 5.9: 2D contour plots of H field in yz plane, x = 50 mm

variation describes the variance of the magnetic field strength of each ROI slice and thus can serve as a metric of the field homogeneity. Only the Gosper coil had a smaller coefficient of variation than the reference coil, and particularly only in the region below 18 mm. This can be seen in figure 5.10. Thus, the field homogeneity of the fractal coils are not better than that of the reference coil, except for that of the Gosper coil.

Electric field analysis

An analysis of the electric field is also prudent to ensure patient safety. The presence of a strong electric field results in high amounts of energy being absorbed by the human body, leading to localized heating and the potential for RF burns to the patient.

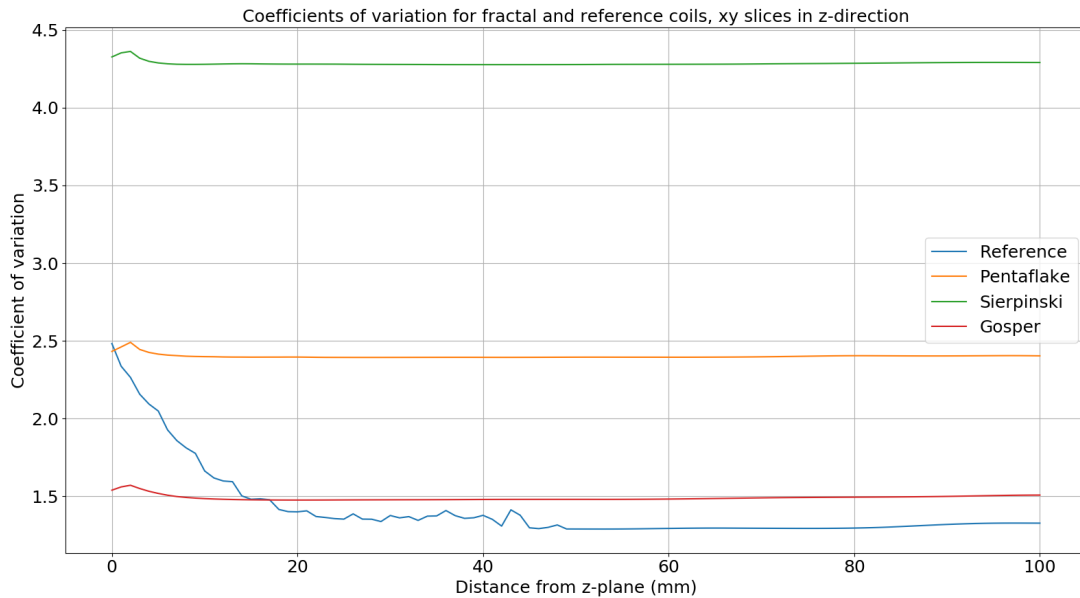


FIGURE 5.10: Coefficients of variation of each coil as a function of distance from the xy -plane in the z -direction

The Health Canada Canadian Safety Code 6 (Health Canada 2011) is a guideline for the maximum permissible electric field exposure to the human body. The Canadian Safety Code 6 guidelines also describe the maximum specific absorption rate (SAR) limits. The specific absorption rate is a limit of the rate at which electromagnetic radiation is absorbed by the human body. The code specifies that SAR limits take precedence over that of field strength limits but allows that in cases where SAR measurements are impractical, the field strength limits can be used instead. In the case of the simulations, only the electric and magnetic field strengths were measured and as such, the field limits will be used in the analysis of the coils.

The safety code limits the electric field strength in a controlled environment to 53.25 V/m for a frequency of 35.3 MHz over a period of six minutes. For each of the coils, the maximum electric field strength in 100 mm by 100 mm xy slices at a distance z above the coil is depicted in figure 5.11. The maximum value of the electric field strength

for each coil is outlined in table 5.3. The maximum for each field supersedes the 53.25 V/m limit in the reference coil, Sierpinski, and Gosper coils, while it is lower in the pentaflake coil. Surpassing the limit may seem like an issue in the Gosper, Sierpinski, and reference coils, however this is not an issue as this maximum occurs at the surface of the coil and the acquisition time for the MRI is shorter than the six minutes. If used in a clinical application, the surface coil is separated from the patient by a thin layer of foam for comfort. Furthermore, if this was ever to be used in a clinical setting, hyperpolarized Xe scanning is acquired using a breath hold on the order of 12 to 15 seconds, well below that of the six minute exposure limit. Thus the time-averaged power over any six minute period is safe in accordance to Canadian Safety Code 6. All this being said, there are other variables not being fully considered that include specific/unique pulse-sequence dependent parameters that are beyond the scope of this body of work.

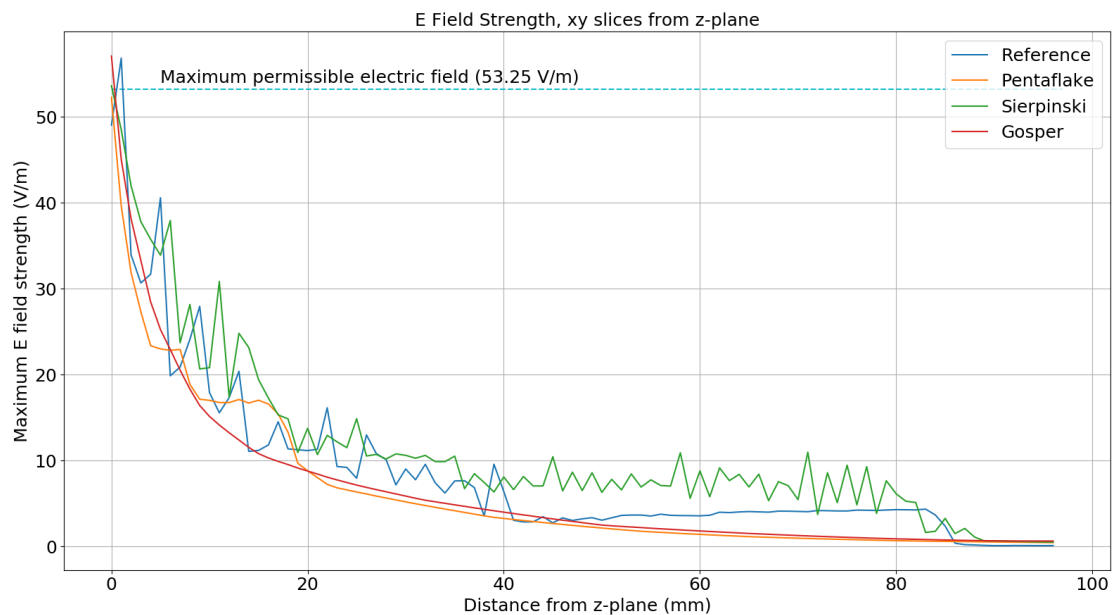


FIGURE 5.11: Maximum electric field (V/m) as a function of distance from the z-plane (mm)

Coil	Maximum electric field strength (V/m)
Reference	56.85
Sierpinski	53.63
Pentaflake	52.28
Gosper	57.09

TABLE 5.3: Table of maximum electric field strength (V/m) for fractal and reference coils

5.2 Experimental Results

5.2.1 Fabricated Coil Analysis

Figure 5.12 depicts the measured reflection coefficients for each of the constructed, tuned, and matched fractal coils. Figure 5.13 depicts the same, but on a Smith chart. All four of the constructed coils show a good match (≤ -15 dB) at the Larmor frequency for ^{129}Xe and also have an impedance close to 50Ω .

The coils were tested using a 3T MRI scanner at the Imaging Research Centre at St. Joseph’s Healthcare in Hamilton, Ontario (*GE Healthcare 2020*). A high-pressure ^{129}Xe thermal phantom (*Polarean Imaging plc 2020*) was used as the signal source. The coils were placed into the MRI, aligned such that the B_1^+ field would be perpendicular to the main magnetic field, B_0 , and the thermal phantom placed atop the coil. A thermal phantom contains a mixture of ^{129}Xe and nitrogen gas. This mixture is not hyperpolarized and is used mainly for quality assurance. The FID of the phantom was measured from a slice located 5 cm above the coils. Figure 5.14 shows the spectrum of the FID. Table 5.4 shows the signal to noise ratio of each coil as calculated using equation 4.2.

As per simulations above, the Gosper and pentaflake coils showed an increase in SNR over that of the reference coil. The Sierpinski coil had a lower noise floor as well

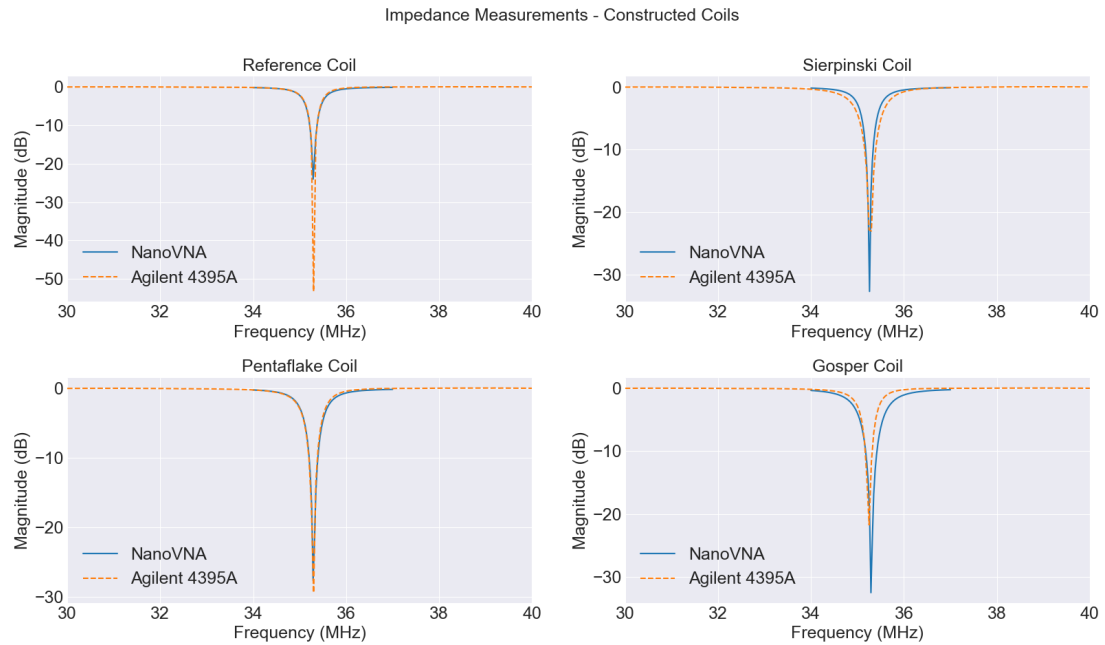


FIGURE 5.12: Comparison of $|S_{11}|$ (dB) measurement of constructed coils using both NanoVNA and Agilent 4395A, top-left: reference, top-right: Sierpinski, bottom-left: pentaflake, bottom-right: Gosper

Coil	SNR
Reference	1.99
Sierpinski	1.40
Pentaflake	2.97
Gosper	2.84

TABLE 5.4: Table of measured SNR results for each coil

as a lower spectral power peak, leading to a lower SNR compared to the reference coil. The SNR was 2.97 and 2.84 for the pentaflake and Gosper coils respectively, while the reference and Sierpinski coils had an SNR of 1.99 and 1.40. In standard imaging of the head using hydrogen, the SNR ranges from 22 to 218 (Dietrich et al. 2007), while in 3T xenon ventilation imaging, the SNR is about 36 to 51 (Xu et al. 2012). Note that the sample from which the experimental signal was acquired used non-hyperpolarized xenon and thus affects the SNR measurement.

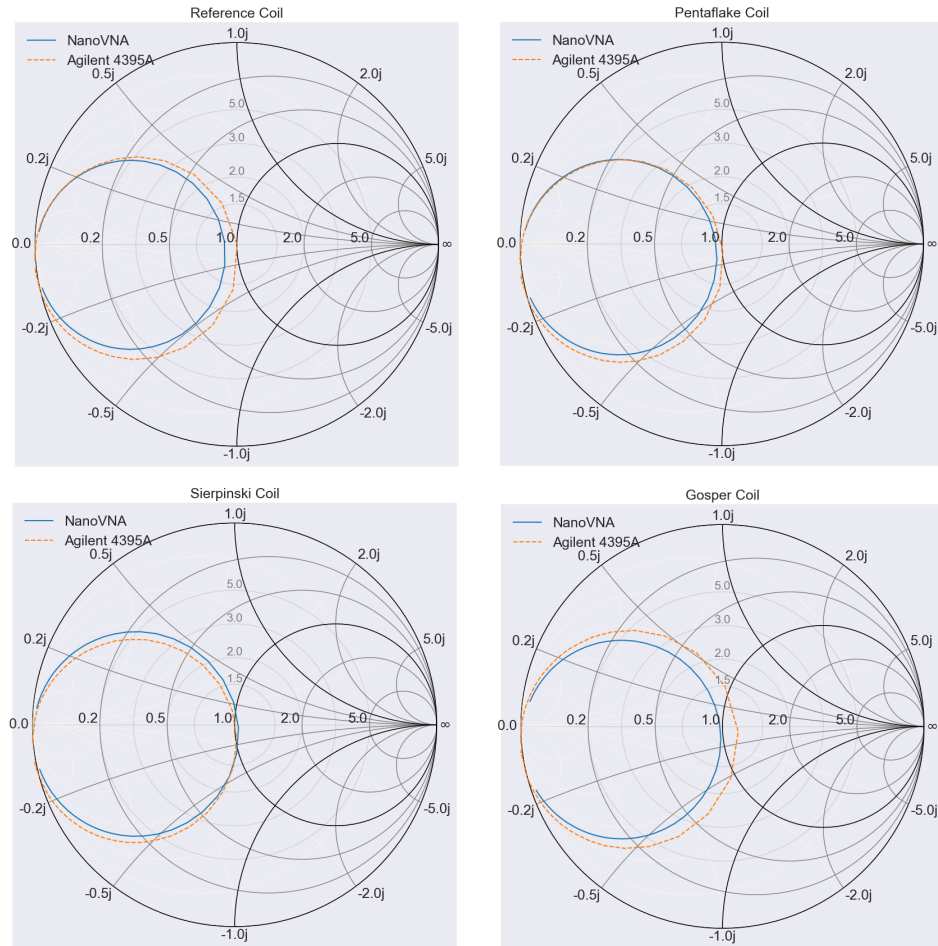


FIGURE 5.13: Comparison of impedance measurement (Smith chart) of constructed coils using both NanoVNA and Agilent 4395A, top-left: reference, top-right: pentaflake, bottom-left: Sierpinski, bottom-right: Gosper

To verify homogeneity, an image of the phantom should be reconstructed and the high-contrast regions would be compared to the background region of the image. Unfortunately, this procedure requires hyperpolarized xenon and due to circumstances beyond the control of the author, this could not be performed. Thus, the homogeneity of the magnetic field could not be verified and simulations must be considered as the result.

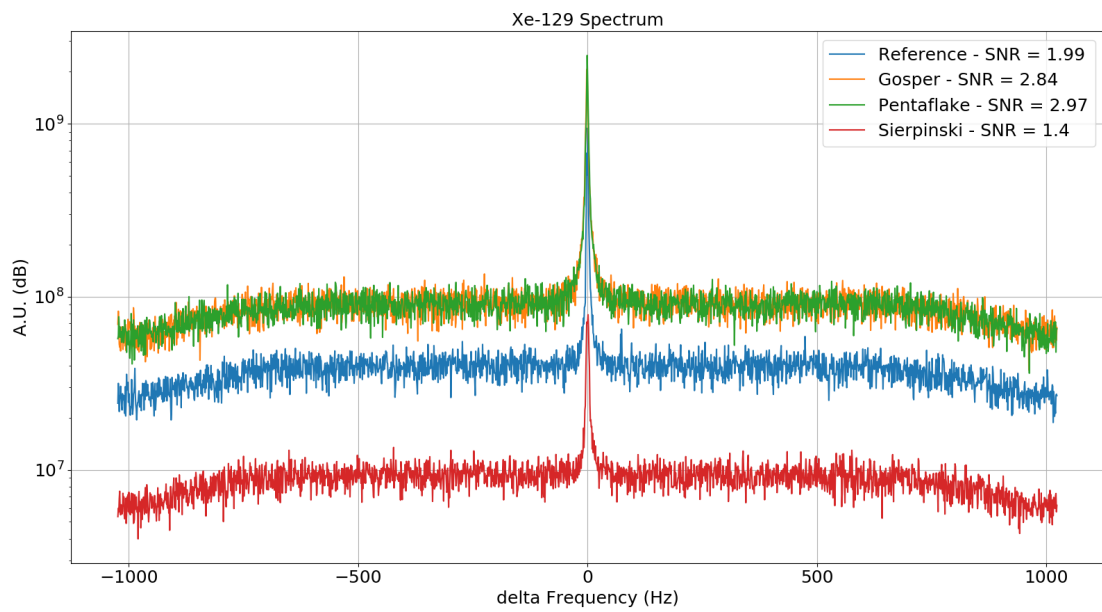


FIGURE 5.14: Comparison of FID signal power spectra, with measures of SNR between each coil

Chapter 6

Conclusion and Future Work

The goal of this thesis was to answer two questions related to the fractal geometry of coils and their performance in an MR imaging application.

The first question was whether a fractal coil geometry can produce a stronger magnetic field (and therefore better signal to noise ratio) than standard coil geometries. In the research performed, Gosper, pentaflake, and Sierpinski coils were shown in simulations to have stronger magnetic fields than that of a reference coil. Simulations suggest an improvement of approximately double the magnetic field strength using the Gosper and pentaflake fractal coils. In experimental validation, the acquired SNR improvement was only about 1 dB. The Sierpinski fractal performed poorly in validation experiments, with an SNR decrease of about 0.6 dB. This may have been due to the more compressed shape of the fractal relative to that of the more annular-like Gosper and pentaflake.

The second question was whether fractal coils have a more homogeneous field than that of a reference coil. Simulations of the magnetic field distribution suggested that

Gosper fractal coil has a more homogeneous field and can avoid the “null zone” associated with the empty portion within the centre of a circular coil. The simulations suggest that the space-filling fractal geometry of the traces on the fractal coils manifests as a more homogeneous field. Experimental validation unfortunately could not be performed.

Fractal coils of the Gosper and pentaflake designs seem to offer improvements in both magnetic field strength and B_1^+ magnetic field uniformity when compared to a reference coil.

6.1 Future Improvements

Future work should be aimed at investigating more fractal geometry shapes and evaluating whether they can perform well when used in MRI scanning. The negative result of the Sierpinski fractal and positive results of the Gosper and pentaflake fractals suggest that there may be more designs that have similar properties. Additionally, the experimental verification of the homogeneity of the coils could not be performed and thus a verification is a necessity in order to strengthen the obtained results.

The Koch-shaped fractal patent (Ha et al. [2014](#)) suggests that fractal antennas have less inductive coupling to each other, and thus may be used in coil arrays. Of course transmit/receive surface coils have limited in actual clinical MRI systems. For routine proton-based MRI, scanners typically use a homogeneous transmit coil and separate receive RF coils. For example, the main transmit “body” coil is a birdcage type design and receive elements are arrays of overlapping surface coils. For hyperpolarized Xe ventilation imaging a large birdcage transmit/receive coil is placed inside the MRI

scanner, typically with a diameter close to that of the full bore. Recently, however, homogeneous Xe transmit coils and separate arrays of receive-only surface coils have been developed (thus mimicking what's done in proton imaging) for lung imaging. Coil-to-coil mutual coupling was not investigated in the process of this current research. But based on the current direction of this form of lung imaging application of fractal-based receive arrays may lead to improvement and thus warrant investigation. It may be that fractal based coils could be of use in such receive arrays and thus would be a valuable avenue of further investigation.

Appendix A

Chapter 3 Supplement

A1 OpenSCAD L-system generator

LISTING A.1: Listing for fractal geometry generator in OpenSCAD

```
/* L-system OpenSCAD library by Hans Loeblich  
Modified by Jimmy - 2019  
*/  
  
$fn=12;  
rounded = true;  
  
color([0.863, 0.447, 0.059])  
// segmented_line([0,0], [10,10]);  
// translate([0, 0, 0])  
  
// peano_curve(n=2, tree=true);  
// gosper_curve(n=3, tree=true);  
// hilbert_curve(n=3, tree=true);  
// hilbert_curve(n=4, tree=true);  
  
// scale([2, 2, 0.035])  
arrowhead(n=5);  
  
// scale([5.8, 5.8, 0.035])  
// moore_curve(n=3, tree=true, w=0.0113);  
// moore_curve(n=3, tree=true, w=0.06);  
  
// scale([6.8, 6.8, 0.035])
```

```
//flowsnake(n=2,w=0.1);

//koch_ring(n=2, angle=60, tree=true);
//ring(d=45);
//substrate();

module arrowhead(n=2, angle=60, tree=true) {
    //translate([-4.5, 2.5])
    L_system_lines([[ "X", "YF+XF+Y", [ "Y", "XF-YF-X" ]], "XF", n, angle);
}

module flowsnake(n=2, angle=60, w=0.4, tree=true) {
    //translate([-4.5, 2.5])
    L_system_lines([[ "F", "F-F+F" ]], "F+F+F+F+F+", n, angle, w);
}

module substrate() {
    scale([1, 1, 0.5])
    color("green")
    square([20, 20], center=true);
}

module ring(d=1, t=2.5) {
    scale([1,1, 0.25])
    difference(){
        circle(d, $fn=50);
        union() {
            //square([10,t/2], center=true);
            circle(d-t, $fn=50);
        }
    };
}

module koch_ring(n=2, angle=60, tree=true) {
    translate([-4.5, 2.5])
    L_system_lines([[ "F", "F-F++F-F" ]], "F++F++F", n, angle);
}

module hilbert_curve(n=4, angle=90, w=0.4, tree=false) {
    L_system_lines([[ "A", "-BF+AF+FB-", [ "B", "+AF-BFB-FA+" ]], "A", n, angle, w, tree=true);
}

module moore_curve(n=4, angle=90, w=0.2, tree=false) {
    translate([-7.5, 0])
    L_system_lines([ [ "L", "-RF+LFL+FR-", [ "R", "+LF-RFR-FL+" ]], "LFL+F+LFL", n, angle, w, tree=true);
}

module peano_curve(n=3, angle=90, w=0.4, tree=false) {
    L_system_lines([[ "L", "LFRFL-F-RFLFR+F+LFRFL" ], [ "R", "RFLFR+F+LFRFL-F-RFLFR" ]], "L", n, angle, w, tree=true);
}
```

```

module gosper_curve(n=4, angle=60, w=0.4, tree=false) {
    // final pass, convert A and B to (F)orward instructions
    final_pass_rules = [{"A", "F"}, {"B", "F"}];
        translate([0, -10])
    L_system_lines([{"A", "A-B--B+A++AA+B-"}, {"B", "+A-BB--B-A++A+B"}],
    "A", n, angle, w, final_pass_rules, tree=tree);
}

module koch_curve(n=4, angle=60, w=0.4, tree=false) {
    L_system_lines([{"F", "F-F++F-F"}], "F", n, angle, w, tree=tree);
}

module koch_snowflake(n=4, angle=60) {
    L_system_polygon([{"F", "F-F++F-F"}], "F++F++F", n, angle);
}

module quadratic_type1_koch(n=4, angle=90, w=0.4, tree=true) {
    L_system_lines([{"F", "F-F+F+F-F"}], "F", n, angle, w, tree=tree);
}

module quadratic_type2_koch(n=4, angle=90, w=0.4, tree=true) {
    L_system_lines([{"F", "F-F+FF-F-F+F"}], "F", n, angle, w, tree=tree);
}

module sierpinski_triangle(n=5, angle=120, w=0.4, tree=true) {
    // for drawing purposes, G is replaced with F
    final_pass_rules = [{"G", "F"}];
    L_system_lines([{"F", "F-G+F+G-F"}, {"G", "GG"}], "F-G-G", n, angle, w, final_pass_rules, tree=tree);
}

module sierpinski_arrowhead(n=6, angle=60, w=0.4) {
    L_system_lines([{"X", "YF+XF+Y"}, {"Y", "XF-YF-X"}], "XF", n, angle, w);
}

///  

module L_system_lines(rules, start, n, angle=90, w=0.4, final_pass_rules, tree=true) {
    if (tree) {
        echo("Tree");
        instrs = L_system(rules, start, n, final_pass_rules, tree);
        //echo(instrs);
        tree_path = create_tree_path(instrs, angle);
        //echo(tree_path);
        dfs_segmented_line(tree_path, w);
        if (rounded) translate(last_2dpoint(tree_path)) circle(d=w);
    } else {
        echo("No_Tree");
        instrs = L_system(rules, start, n, final_pass_rules, tree);
        echo(instrs);
    }
}

```

```

    path = create_path(instrs , angle);
    echo(path);
    segmented_line(path , w);
}
}

module L_system_polygon(rules , start , n , angle=90 , final_pass_rules) {
    instrs = L_system(rules , start , n , final_pass_rules , false);
    path = create_path(instrs , angle);
    //echo(path);
    polygon(path);
}

// traverse a tree of 2d points , depth first , drawing lines between them
module dfs_segmented_line(root , w , prev , i=0) {
    l = len(root);
    if (l > 0) {
        if (i < l) {
            curr = root[i];
            if (is_2dpoint(curr)) {
                if (prev != undef) {
                    //echo(prev , " to " , curr);
                    line(prev , curr , w);
                }
            } else {
                //newlast = last_2dpoint(second);
                dfs_segmented_line(curr , w , prev , 0);
            }
            dfs_segmented_line(root , w , last_2dpoint(curr) , i+1);
        }
    }
}

// works on long lists of points
module segmented_line(points , w=0.1) {
    // OpenSCAD doesn't allow ranges > 10000 in modules,
    // so limit is used to split very large segmented lines into manageable chunks
    limit = 9999;
    l = len(points);
    imax = floor((l-2) / limit);
    for (i = [0:1:imax]) {
        jmin = i*limit;
        jmax = min(jmin + limit - 1 , (l-2));
        for (j = [jmin:1:jmax]) {
            line(points[j] , points[j+1] , w);
        }
    }
    if (rounded) translate(points[1]) circle(d=w);
}

module line(A , B , w=0.1) {

```

```

xa = A[0];
ya = A[1];
xb = B[0];
yb = B[1];
dx = (xb - xa);
dy = (yb - ya);
d = sqrt(dx*dx + dy*dy);
a = atan2(dy, dx);
translate(A) {
    if (rounded) circle(d=w);
    rotate([0,0,a]) translate([0,-w/2]) square([d,w]);
}
}

function is_string(x) = str(x)==x;
function is_char(x) = x == x[0]; // works except for undef
function is_number(x) = x[0]==undef;
function is_2dpoint(p) = (len(p) == 2) && is_number(p.x) && is_number(p.y);
function is_2dpoint_list(list) = _is_2dpoint_list(list, len(list));
function _is_2dpoint_list(list, i) = is_2dpoint(list[i]) ? ((i==0) ? true : _is_2dpoint_list(list, i-1)) : false;

// traverse tree last elements until 2d point is found
function last_2dpoint(root) = is_2dpoint(root) ? root : last_2dpoint(root[len(root)-1]);

// Take a list of strings and return the concatenation of all strings
function join(strs, i=0) = (i == len(strs)-1 ? strs[i] : str(strs[i], join(strs, i+1)));

// take a string, and a second string representing all valid characters.
// return only the valid characters from the first string
function filter_string(string, valids) =
    let(imax = len(string)-1, jmax = len(valids)-1)
    join([for (i = [0:imax], j = [0:jmax]) let (ch = string[i]) if (ch == valids[j]) ch]);

// wrapper for the recursive function, formats the final pass rules for efficient usage
function L_system(rules, start, n, final_pass_rules=[], tree=true) =
    let(
        // string of all chars that are allowed as drawing instructions
        valid_chars = "F-+",
        imax = len(rules)-1,
        jmax = len(final_pass_rules)-1,
        final_rules = [for (rule = rules)
            let(
                r_val = rule[1],
                kmax = len(r_val),
                // run final pass rules over original rules
                new_r_val = (len(final_pass_rules) > 0) ?
                    join([for (k = [0:kmax])
                        let(ch = r_val[k], results = quiet_search(ch, final_pass_rules, 0, 0)
                            len(results) == 0 ? ch : final_pass_rules[results[0]][1]]) :
                    r_val
            )
        ]
    )

```



```

        [rule[0], filter_string(new_r_val, valid_chars)]
    ]
)
tree ?
_L_system_tree(rules, start, n, final_rules) :
_L_system(rules, start, n, final_rules);

// recursive function that applies replacement rules
// keeping data in a tree like structure helps guarantee that max recursion limit is not reached
function _L_system_tree(rules, val, n, final_rules) =
    let(imax = len(val)-1)
    n == 0 ? val :
    [for (i = [0:imax])
        let(
            ch = val[i],
            rs = (n == 1) ? final_rules : rules,
            results = quiet_search(ch, rs, 0, 0) )
        len(results) == 0 ?
            ch :
            [_L_system_tree(rules, rs[results[0]][1], n-1, final_rules)]
    ];

// Iterate an L-system, recursively apply replacement rules to the string, n times
function _L_system(rules, val, n, final_rules) =
    let(imax = len(val)-1)
    n == 0 ? val :
    join([
        for (i = [0:imax])
            let(
                ch = val[i],
                rs = (n == 1) ? final_rules : rules,
                results = quiet_search(ch, rs, 0, 0) )
            len(results) == 0 ?
                ch : // no matching rule, character is a constant
                _L_system(rules, rs[results[0]][1], n-1, final_rules)
    ]);

// Take "turtle instructions" and convert into a list of points on a curve
// this is the user-friendly wrapper for the recursive function
function create_path(instrs, angle=90, pos=[0,0], heading=0) =
    let(
        imax = len(instrs)-1,
        // strip any extraneous characters that are not used as drawing instructions
        // before calling the recursive function, in order to reduce the i^2 load of concat for every element
        filtered = [for (i = [0:imax], valid = ["F", "-", "+"]) let (instr = instrs[i]) if (instr == valid) instr],
        l = len(filtered)
    )
    _create_path(filtered, l, angle, pos, heading);

// thanks to InPhase for helping re-write this to behave better under heavy recursion

```

```

function _create_path(instrs, leninstrs, angle, pos, heading, i=0, prepend=[]) =
  (i >= leninstrs) ?
    [ for (a=[[pos], prepend]) for (b = a) b ] :
    _create_path(instrs, leninstrs, angle,
      (instrs[i] == "F") ? pos + [cos(heading), sin(heading)] : pos,
      (instrs[i] == "-") ? heading + angle : (instrs[i] == "+") ? heading - angle : heading,
      i+1,
      (instrs[i] == "F") ? concat([pos], prepend) : prepend);

function create_tree_path(root, angle=90, pos=[0,0], heading=0) =
  let( result = _create_tree_path(root, angle, len(root), 0, [pos, heading, [] ])
    [pos, result[2]];

// Due to how L_system_tree generates its output, and how create_tree_path processes it,
// max recursion depth is roughly on the order of (n + m),
// where n is number of iterations of the system and m is length of the longest rule for a given system
function _create_tree_path(root, angle, l, i=0, vars) =
  let(
    pos = vars[0],
    heading = vars[1],
    points = vars[2]
  )
  // pos, heading, points=[0,0]
  (i < l ?
    let(node = root[i])
      (is_char(node) ?
        // Found character
        (node == "F" ?
          let(newpos = pos + [cos(heading), sin(heading)])
            _create_tree_path(root, angle, l, i+1, [newpos, heading, concat(points, [newpos])] ) :
          (node == "-" ?
            _create_tree_path(root, angle, l, i+1, [pos, heading+angle, points]) :
          (node == "+" ?
            _create_tree_path(root, angle, l, i+1, [pos, heading-angle, points]) :
            _create_tree_path(root, angle, l, i+1, vars) // node is unused character, ignore and go to next index
          )
        )
      ) :
    let( next = _create_tree_path(node, angle, len(node), 0, [pos, heading, []]) )
      // node is not a character, so must be a list, go deeper
      _create_tree_path(root, angle, l, i+1, [next[0], next[1], concat(points, [next[2]])] )
    ) :
  // i >= l
  vars
);

// hack to avoid warning messages every time the search function misses
function quiet_search(m, s, n, i) =
  let(
    t = (i == undef) ?
      search(m, str(s.m), 0)[0] :

```

```
    search(m, concat(s, [[for(j=[0:1:i]) m ]]), 0, i)[0],  
    maxi = (n == 0) ? len(t)-2 : min(len(t)-2, n)  
  )  
  len(t) > 1 ? [ for (i=[0:1:maxi]) t[i] ] : [];
```

Bibliography

- Analog Devices (2020). *Analog Device - RF Impedance Matching Calculator*. <https://www.analog.com/en/design-center/interactive-design-tools/rf-impedance-matching-calculator.html>.
- Ansys HFSS R19.2 (2018). *Ansys HFSS R19.2 - High Frequency Electromagnetic Field Simulation Software*. <http://www.ansys.com/products/electronics/ansys-hfss/>.
- ARRL Antenna Book (2019). American Radio Relay League. ISBN: 978-1-62595-114-4.
- Autodesk (2020). *Autodesk Fusion360*. <http://www.autodesk.com/>.
- AVX Corporation (2020). *American Technical Ceramics*. <http://www.avx.com>.
- Balanis, C. (2016). *Antenna Theory: Analysis and Design*. John Wiley & Sons, Inc., Hoboken, New Jersey. ISBN: 978-1118642061.
- Biederer, J., Beer, M., Hirsch, W., Wild, J., Fabel, M., Puderback, M., and Beek, E. van (Aug. 2012). MRI of the lung (2/3). Why .. when .. how? 3(4), 355–371.
- Brown, R., Cheng, Y., Haacke, E., Thompson, M., and Venkatesan, R. (2014). *Magnetic Resonance Imaging: Physical Principles and Sequence Design*. John Wiley & Sons, Inc., Hoboken, New Jersey. ISBN: 978-0-471-72085-0.
- Charras, J. (2020). *KiCad*. <http://www.kicad-pdb.org/>.
- Cohen, N. (1995). Fractal Antennas, Part 1 - Introduction to the Fractal Quad. *Communications Quarterly* 5(3). ISSN: 1053-9433.

Bibliography

- Corea, J., Lechene, P., Lustig, M., and Arias, A. (Aug. 2017). Materials and Methods for Higher Performance Screen-Printed Flexible MRI Receive Coils. *Magnetic Resonance in Medicine*, 775–783.
- Dietrich, O., Raya, J., Reeder, S., Reiser, M., and Schoenberg, S. (2007). Measurement of signal-to-noise ratios in MR images: influence of multichannel coils, parallel imaging, and reconstruction filters. *Journal of Magnetic Resonance Imaging* 26(2), 375–385.
- Dobkin, D., Weigand, S., and Iyer, N. (June 2007). Segmented magnetic antennas for near-field UHF RFID. 50, 96–102.
- Fujita, H., Zheng, T., Yang, X., Finnerty, M., and Handa, S. (July 2013). RF Surface Receive Array Coils: The Art of an LC Circuit. *Journal of Magnetic Resonance Imaging*, 12–25.
- GE Healthcare (2020). *Discovery™ MR750, a 3.0T system*. <http://www.gehealthcare.com>.
- GE Healthcare (2020). GE Healthcare.
- Gruber, B., Froeling, M., Leiner, T., and Klomp, D. (Sept. 2018). RF coils: A practical guide for nonphysicists. *Journal of Magnetic Resonance Imaging* 48(3), 590–604.
- Ha, S., Roeck, W., and Nalcioglu, O. (2014). *Fractal RF coils for magnetic resonance imaging - U.S. Patent 9784806B2*.
- Health Canada (2011). Limits of Human Exposure to Radiofrequency Electromagnetic Energy in the Frequency Range from 3 kHz to 300 GHz - Safety Code 6. *Industry Canada Technical Guide*.
- Keltner, J. R., Carlson, J. W., Roos, M. S., Wong, S. T. S., Wong, T. L., and Budinger, T. F. (1991). Electromagnetic fields of surface coil in vivo NMR at high frequencies. *Magnetic Resonance in Medicine* 22(2), 467–480.

Bibliography

- Kinel, M. and Wolf, C. (2019). *OpenSCAD*. <http://www.openscad.org/>.
- Lemus, O. M. D., Konyer, N. B., and Noseworthy, M. D. (2018). Micro-strip Surface Coils Using Fractal Geometry for ^{129}Xe Lung Imaging Applications. *International Society for Magnetic Resonance in Medicine - Abstracts* (1713).
- Morey, A., Bhujade, S., Bhuiya, T., Thakur, S., and Pandey, T. (May 2015). Design and development of surface coil for 1.5T MRI scanner. *International Conference on Smart Technologies and Management for Computing, Communication, Controls, Energy and Materials*.
- Pakkathillam, J. K., Kanagasabai, M., Varadhan, C., and Sakthivel, P. (2013). A Novel Fractal Antenna for UHF Near-Field RFID Readers. *IEEE Antennas and Wireless Propagation Letters* 12.
- Polarean Imaging plc* (2020). Polarean Imaging plc.
- Roos, J., McAdams, H., Kaushik, S., and Driehuys, B. (May 2015). Hyperpolarized Gas MRI: Technique and Applications. 23(2), 217–229.
- Schulte, R. F., Sacolick, L., Deppe, M. H., Janich, M. A., Schwaiger, M., Wild, J. M., and Wiesinger, F. (2011). Transmit gain calibration for nonproton MR using the Bloch-Siegert shift. *NMR in Biomedicine* 24(9), 1068–1072.
- Sohn, S., DelaBarre, L., Gopinath, A., and Vaughan, J. (Oct. 2014). Design of an Electrically Automated RF Transceiver Head Coil in MRI. *IEEE Transactions on Biomedical Circuits and Systems* 9(5), 725–732.
- Stutzman, W. and Thiele, G. (2012). *Antenna Theory and Design*. John Wiley & Sons, Inc., Hoboken, New Jersey. ISBN: 978-0470576649.
- Tao, Y., Yang, E., Dong, Y., and Wang, G. (2017). Design of UHF fractal antenna for localized near-field RFID application. *Microwave and Optical Technology Letters* 59(6).

Bibliography

- Vaidya, M., Collins, C., Sodickson, D., Brown, R., Wiggins, G., and Lattanzi, R. (Feb. 2016). Dependence of B_1^+ and B_1^- Field Patterns of Surface Coils on the Electrical Properties of the Sample and the MR Operating Frequency. 46(1), 25–40.
- Vincent, J. and Rispoli, J. (July 2019). Stitching Stretchable Radiofrequency Coils for MRI: A Conductive Thread and Athletic Fabric Approach. *Conference proceedings - IEEE engineering in medicine and biology society*, 6798–6801.
- Vishay Intertechnology Incorporated (2020). *Vishay*. <http://www.vishay.com>.
- Walker, T. (July 2010). Fundamentals of Spin-Exchange Optical Pumping. *Journal of Physics: Conference Series* 294.
- Xu, X., Norquay, G., Parnell, S., Deppe, M., Ajraoui, S., Hashoian, R., Marshall, H., Griffiths, P., Parra-Robles, J., and Wild, J. (2012). Hyperpolarized ^{129}Xe gas lung MRI—SNR and T_2^* comparisons at 1.5 T and 3 T. *Magnetic Resonance in Medicine* 68(6).
- Yan, X., Gore, J., and Grissom, W. (Aug. 2018). Self-decoupled radiofrequency coils for magnetic resonance imaging. *Nature Communications* (3481).
- Zhurbenko, V. (2016). Optimal Value of Series Capacitors for Uniform Field Distribution in Transmission Line MRI Coils. *Journal of Sensors*.